

Phase-free Dynamic Movement Primitives Applied to Kinesthetic Guidance in Robotic Co-manipulation Tasks

Giovanni Braglia[✉], Davide Tebaldi[✉], and Luigi Biagiotti[✉]

Abstract—When there is a need to define and adapt a robotic task based on a reference motion, Dynamic Movement Primitives (DMP) is a standard and efficient method for encoding it. The nominal trajectory is typically obtained through a Programming by Demonstration (PbD) approach, where the robot is taught a specific task through kinesthetic guidance. Subsequently, the motion is reproduced by the manipulator in terms of both geometric path and timing law. The basic approach for modifying the duration of the execution involves adjusting a time constant characterizing the model.

On the contrary, the goal of this paper is to achieve complete decoupling between the geometric information of the task, encoded into the DMP, and the phase law governing the execution, allowing them to be chosen independently. This enables the optimization of the task duration to satisfy constraints such as velocity or acceleration or even to define a phase law dependent on external inputs, such as the force applied by a user in a co-manipulation task. As an example, this mechanism will be exploited to define a rehabilitation activity where the cobot assists humans in performing various pre-planned exercises.

Index Terms—Physical Human-Robot Interaction, Motion and Path Planning, Rehabilitation Robotics, Dynamic Movement Primitives.

I. INTRODUCTION

IN recent years, the interest in collaborative robotics has been significantly rising, as robots are starting to work with humans rather than performing separate tasks [1], [2]. In this case, we usually refer to Human-Robot Interaction (HRI) every time we address novel algorithms and techniques to enhance human-robot communication, coexistence and collaboration in various settings [3]–[6].

While robots are recently gaining high popularity, a way to bridge the required technical knowledge for robotic programming and its access to non-expert users is still missing [7], [8]. Possible solutions are given by techniques such as Imitation Learning [9], which learn by observing

The work was partly supported by the University of Modena and Reggio Emilia through the action FARD (Finanziamento Ateneo Ricerca Dipartimentale) 2022 and 2023, and funded under the National Recovery and Resilience Plan (NRRP), Mission 04 Component 2 Investment 1.5 – NextGenerationEU, Call for tender n. 3277 dated 30/12/2021 Award Number: 0001052 dated 23/06/2022.

The authors are with the Engineering Department Enzo Ferrari of the University of Modena and Reggio Emilia (Unimore), Via Pietro Vivarelli 10, 41125, Modena, Italy. Contacts: {giovanni.braglia, davide.tebaldi, luigi.biagiotti}@unimore.it

and mimicking human or expert behavior. Often referred to as Programming by Demonstration (PbD) [8], these methods involve a demonstration phase and rely on encoding, planning and control strategies to correctly reproduce the desired task [10]–[12].

One of the most widespread encoding/planning techniques in the literature is Dynamic Movement Primitives (DMP) [13], which was first introduced in [14] as a way to encode motor movement with convenient stability properties. DMP consists of a mass-spring-damper system with the addition of a forcing term, allowing to shape the attractor landscape according to the desired dynamics [15], and can be classified into rhythmic or discrete DMP, depending on whether the attractor system is a limit cycle or a point [13], respectively. In this paper, we deal with the discrete version of DMP which, in its basic formulation, can be expressed as follows [13], [15]:

$$\tau \dot{z}(t) = \alpha[\beta(g - y(t)) - z(t)] + f(s(t)), \quad (1)$$

$$\tau \dot{y}(t) = z(t), \quad (2)$$

$$\tau \dot{s}(t) = -\delta s(t). \quad (3)$$

Equations (1)-(2) are referred to as the Transformation System (TS), whereas Eq. (3) is referred to as the Canonical System (CS). Parameter τ is a time constant, α and β are positive parameters chosen such that the TS is critically damped (i.e. $\beta = \alpha/4$), g is the target goal and the forcing term $f(s(t))$ shapes the generated trajectory $y(t)$ according to the dynamics of the TS. Whenever $f(s(t)) = 0$, the TS of Eqs. (1)-(2) represents a globally stable second-order linear system, that can be rewritten as:

$$\tau^2 \ddot{y}(t) + \alpha \tau \dot{y}(t) + \alpha \beta (y(t) - g) = f(s(t)), \quad (4)$$

with a unique equilibrium point located in $(z(t), y(t)) = (0, g)$. Note that Eq. (4) models a mass-spring-damper mechanical system with unitary mass, friction coefficient α and spring stiffness $\alpha \beta$.

The Canonical System is generally a first-order system representing the evolution of the phase variable $s(t)$, with δ being a positive constant [15]. The forcing term $f(s(t))$ in (1) is typically expressed as the linear combination of radial basis functions [14]:

$$f(s(t)) = \sum_{i=1}^N \omega_i \phi_i(s(t)) \cdot s(t) \cdot (g - y_0), \quad (5)$$

where

$$\phi_i(s(t)) = \frac{b_i(s(t))}{\sum_{j=1}^N b_j(s(t))}, \quad b_i(s(t)) = \exp\left(\frac{-(s(t)-c_i)^2}{2h}\right). \quad (6)$$

Note that, since $s(t) \rightarrow 0$ when $t \rightarrow \infty$ according to the CS dynamics in (3), the impact of $f(s(t))$ in the TS dynamics in (1)-(2) tends to disappear, as $f(s(t)) \rightarrow 0$ in (5). The constant $(g - y_0)$ is a modulation term that enables the TS to be an orientation-preserving homeomorphism with respect to changes in the initial and goal positions y_0 and g , respectively [14], [16]. Finally, ω_i are the weight coefficients calculated by Locally Weighted Regression (LWR) [17] minimizing the quadratic error with respect to the nominal forcing term f^* :

$$\omega_i = \operatorname{argmin}_{\omega_i} \sum_{t=0}^{T_f} \phi_i(s(t)) [f^*(t) - \omega_i \xi(t)]^2, \quad (7)$$

where $\xi(t) = s(t)(g - y_0)$ and f^* is computed through the *inverse dynamics* of the TS. This involves inserting the profiles of position, velocity, and acceleration of the reference trajectory $y_r(t), \dot{y}_r(t), \ddot{y}_r(t)$ into (4):

$$f^* = \tau^2 \ddot{y}_r(t) + \alpha \tau \dot{y}_r(t) + \alpha \beta (y_r(t) - g_r), \quad (8)$$

where $g_r = y_r(T_f)$. Here, T_f is the total duration of the reference trajectories $y_r(t)$, and τ is commonly assumed to be unitary. Note that $f(s(t))$ is firstly computed as a linear combination of the reference position profile and its derivatives, and then approximated via a combination of radial basis functions. Moreover, its definition depends on the phase variable $s(t)$ which appears in (5) and (7).

DMP is a simple yet effective encoding technique, featuring useful properties such as stability, time scaling, spatial modulation, and compatibility with additional coupling terms [13], [14], [18]. Due to its compact and versatile formulation, DMP was successfully applied to various tasks, such as tennis swing [15], bi-manual manipulation [19], peg-in-hole [20], among others [5], [21]–[23].

Despite the several interesting researches on DMP, we identified some research branches which, to the best of our knowledge, have not been fully investigated yet. These branches and the contributions we offer are discussed in detail in Sec. III.

The rest of this manuscript is structured as follows. An overview of the state of the art and of the issues when dealing with DMP is given in Sec. II, whereas the contributions of this work are discussed in Sec. III. The adopted DMP formulation is discussed in Sec. IV, while Sec. IV-A describes the proposed Spatial Sampling algorithm which represents the core of the proposed Geometric DMP (GDMP) formulation. Different applications of the GDMP are discussed in Sec. V; specifically, an optimization problem is discussed in Sec. V-A, while a human-in-the-loop application is discussed in Sec. VI for which a passivity analysis is also carried out, to proof the safety of the human-robot interaction. Experimental tests related to the human-in-the-loop application are reported and

discussed in detail in Sec. VII. Conclusions are reported in Sec. VIII.

II. RELATED WORKS

The state trajectories of a dynamical system naturally evolve with time. However, in cases where the dynamical model does not represent a real system, it might be necessary for these trajectories to evolve according to a different time scaling. For instance, scaling the original time by a suitable factor can enhance flexibility, offering advantageous properties like feedback linearizability [24], [25].

In the specific case of DMP, the time law is governed by the Canonical System (CS) in (3), where the variation of the phase variable $s(t)$ can be modulated by properly tuning the parameter τ , thus giving a time-scalable Transformation System (TS) in (1)-(2) and maintaining the topological equivalence of the output trajectories [14], [20], [23]. Choosing the CS in (3) to exhibit an exponential decay ensures that the contribute of $f(s(t))$ in (1), calculated as in (5), fades out when reaching the goal point g [13]. However, this solution inevitably leads to very high weights in (7) when close to the final part of the reference trajectory [26], which can be undesirable when combining multiple DMP together [5], [18], [22]. To cope with this issue, other types of CS were adopted, such as piece-wise linear [26] or sigmoidal-like phase profiles [27].

The key aspect of having a time law governed by the CS in (3) is that the evolution of the trajectory $y(t)$ in the Transformation System (TS) (1)-(2) can be effectively slowed down or speeded up by tuning the parameter τ without introducing any geometric variation in the resulting trajectory $y(t)$ of the DMP [14], [16]. In this case, an issue arises when the trajectory is required to momentarily stop during its reproduction, as this would imply $\tau \rightarrow \infty$. This problem was noted in [15], [28], then further analyzed in [21]. In the latter reference, the scaling factor τ relies on the phase $s(t)$ and is expressed as a combination of basis functions, aiming at acquiring an optimized velocity profile for a bimanual kitchen task.

Many different formulations of the CS in (3) can be found in the literature, to adopt proper time laws for the considered applications. In [29], for instance, a coupling term is used to modulate the task velocity based on the measured contact force with the environment. The task velocity can also be changed as in [28], where non-uniform velocity changes are allowed to move along the trajectory according to the forces and torques applied to the robot. In [30], Iterative Learning Control (ILC) is employed to learn an additional and optimal phase-dependent temporal scaling factor into the DMP equations, whereas an online optimization of the time duration of the task is performed in [23] in order to vary the task velocity, and thus the robot velocity, as a function of the distance from the target. Other works where the time law is modified according to external perturbation on the planned trajectory can be found in [15], [20], [31].

An important aspect when dealing with time laws is the possibility of letting the trajectory move backward and forward between the initial and goal positions, y_0 and g respectively, while preserving the trajectory topology, i.e., allowing $\dot{s}(t)$ to change sign [20], [32]. This feature is called phase reversibility. Even though it offers many benefits in various scenarios [28], the classical DMP formulation in (1)-(3) does not fulfil the phase reversibility requirement [30]. In fact, the restriction on having a strictly monotonic $\dot{s}(t)$ implies that the new time law neither allows the trajectory to be reproduced backward nor to be stopped [25].

The problem of reversibility has been considered in [33] and further investigated in [20], [34], where it has been shown that having a reversible phase can affect the DMP global stability property [28]. In [34], the authors formulate the design requirements for guaranteeing phase reversibility in DMP, which is a desirable property in some DMP formulation [20], [23], [35], [36]. Firstly, a reversible DMP should maintain global stability properties as the original one [34], meaning that y_0 must be an attractor point when moving backward, whereas g must be an attractor point when moving forward. Secondly, the trajectory topology must be preserved when moving forward and backward. Finally, it would be desirable to adopt the same forcing term when progressing along the intended path.

Whenever a new DMP formulation is proposed, it is important to verify that global asymptotic stability is guaranteed. In [34], a candidate for such a system is given by the Logistic Differential Equation (LDE) $\tau\dot{y} = \alpha(y - y_0)(g - y)$. However, it can be demonstrated that the region of global stability of the LDE is restricted to $y \in (y_0, g)$ with $y_0 < g$, while it is not ensured outside [37]. As a consequence, two separate forcing terms are learned to switch along the desired curve whenever the sign of \dot{s} changes [38].

When dealing with phase reversibility, a considerable step forward was provided in [20]. In this work, the authors present a new formulation of the original DMP satisfying all phase reversibility requirements by using a unique forcing term $f(s(t))$, based on a parameterization of the reference trajectory $y_r(t)$ and of its time-derivatives [32], [39]. In this case, there is no need to limit the forcing term $f(s(t))$ by multiplying it by $s(t)$, as the terms $y_r(t)$, $\dot{y}_r(t)$, $\ddot{y}_r(t)$ are bounded by construction and the derivatives tend to zero when the system approaches the initial/goal positions [35]. Additionally, backward reproduction is achieved without impacting the stability of the DMP by simply reversing the sign of the phase velocity $\dot{s}(t)$ [23].

A potential application for reversible DMP is its use as a *virtual fixture* [40] [41] [42]. These fixtures involve predefined paths that constrain the robot's movement without a specified time law. The phase variable $s(t)$ can be adjusted arbitrarily, allowing the system to evolve along these predefined paths. However, the DMP architecture imposes limitations as recorded reference trajectories are affected by the time dependence observed in task demonstrations

[8]. The same issue emerges when multiple demonstrations of the same task are recorded with different time laws and they must be condensed in a unique reference motion. Aligning these demonstrations becomes necessary to extract the related skill [7], [10]. This problem, referred to as *time warping* [43], essentially involves extracting the geometric characteristics of the task.

In this paper, we address the issues detailed in this section by proposing the concept of Geometric DMP (GDMP). The latter is based on the proposal of a new Spatial Sampling algorithm, allowing the introduction of a geometric interpretation for the phase variable $s(t)$. This new phase variable can now be properly chosen depending on the specific application under consideration.

III. METHODOLOGY AND CONTRIBUTIONS

Despite the extensive literature on DMP, as far as we know, there is still no unified framework that allows for arbitrary selection of the Canonical System in (3).

In this work, we employ the DMP formulation proposed in [20] by providing the following new contributions: 1) The proposal of a new Spatial Sampling algorithm. This algorithm allows the conversion of the demonstrated trajectory, which is constantly time-sampled, into a new trajectory which is constantly spatially-sampled. In doing so, the resulting trajectory no longer exhibits the time dependence of the original one and can be expressed as a function of its arc-length parameter, the latter representing the length of the path itself. The resulting spatially-sampled trajectory can now be parameterized as a function of a new phase variable. 2) The decoupling of the phase variable from the time law during the demonstration phase, which is achieved through the introduction of the Spatial Sampling algorithm in 1). The phase variable can now be freely chosen depending on the application and is no longer constrained by CS evolution in (3), thus originating the new concept of “phase-free” DMP. 3) The proposal of the new concept of Geometric DMP (GDMP) thanks to 1) and 2), where the forcing term $f(s(t))$ is computed solely based on geometrical information contained in the demonstrated trajectory, while the phase variable can be chosen independently. Based on the new concept of GDMP, a further contribution of this paper is as follows: 4) the exploitation of the phase-free concept to properly optimize the execution of the trajectory based on a given objective. As a case study, we set up two optimization problems where the objective is to minimize the execution time of the task subject to different constraints. Finally, the introduction of GDMP has led to an additional contribution of this work: 5) the proposal of a human-in-the-loop application, where the stability of the human-robot interaction has been analytically demonstrated by a rigorous passivity and stability analysis. The overall architecture has been validated through several experiments, related to a robotic co-manipulation task which is taken as a case study application.

IV. GEOMETRIC DMP FORMULATION

As mentioned in Sec. III, we employ the DMP formulation proposed in [20], where the forcing term $f(s(t))$ in (4) is computed as:

$$f(s(t)) = \eta f^*(s(t)), \quad (9)$$

being

$$\eta = \frac{g - y(s(0))}{g_r - y_r(0)} \quad (10)$$

a scaling factor that depends on the initial and goal positions of the reference trajectory, $y_r(0)$ and $g_r = y_r(s_f)$ respectively, on the initial configuration of the CS $y(s(0))$ and on the desired goal g . This factor preserves the topology of the curve [16], [23], [36]. The term $f^*(s(t))$ is obtained by substituting a suitable parameterization of the demonstrated trajectory and its derivatives into (4). Therefore, unlike the original formulation of the DMP, where $f^*(s)$ is obtained by approximating a linear combination of the position, velocity, and acceleration profiles of the demonstrated motion with a parametric function based on the dynamics of the TS, in this case, the nominal trajectory is first parameterized using a suitable curve $y^*(s)$. Subsequently, the forcing term $f^*(s)$ is computed as a combination of $y^*(s)$, $\dot{y}^*(s)$, and $\ddot{y}^*(s)$. In more detail, given the sequence of demonstrated positions $y_r(s)$, $s = 0, \dots, s_f$, the coefficients ω_i of parametric function

$$y^*(s(t)) = \sum_{i=1}^N \omega_i \phi_i(s(t)) \quad (11)$$

are determined by minimizing the cost function

$$J = \sum_{t=0}^{T_f} \|y_r(t) - \omega_i \phi_i(s(t))\|^2, \quad (12)$$

with the boundary conditions

$$\sum_{i=1}^N \omega_i \phi_i(0) = y_r(0), \quad \sum_{i=1}^N \omega_i \phi_i(s_f) = y_r(s_f). \quad (13)$$

The radial basis functions $\phi_i(\cdot)$ are defined in (6), and the timing-law $s = s(t) : [0, T_f] \rightarrow [0, s_f]$ is a monotonic function of class C^1 such that $\dot{s}(0) = \dot{s}(T_f) = 0$ and $\ddot{s}(0) = \ddot{s}(T_f) = 0$.

The optimal control problem (12) subject to (13) can be solved using the Lagrange multipliers method [12] as detailed in App. A. The first and second derivatives of the parameterized trajectory $y^*(s(t))$ with respect to time can be computed, once the phase variable $s = s(t)$ has been defined, as

$$\begin{aligned} \dot{y}^*(s(t)) &= \frac{\partial y^*(s(t))}{\partial s(t)} \frac{ds(t)}{dt} = y^{*'}(s(t)) \dot{s}(t), \\ \ddot{y}^*(s(t)) &= \frac{d\dot{y}^*(s(t))}{dt} = y^{*''}(s(t)) \dot{s}^2(t) + y^{*'}(s(t)) \ddot{s}(t), \end{aligned} \quad (14)$$

where the prime and dot notations denote the differentiation with respect to the phase variable s and with respect to time, respectively. Therefore, with the proposed formulation, it is not necessary to know the derivatives of

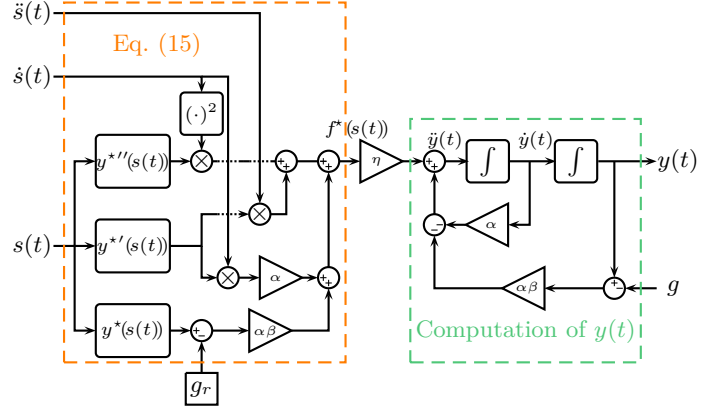


Figure 1: Block-scheme representation of the TS described by (4), incorporating the forcing term (15), which ensures the independence from the phase signal $s(t)$.

the reference trajectory, but only the position profile y_r is sufficient.

Finally, using (9), (11) and (14), one can write the forcing term $f(s(t))$ in (4) as:

$$f(s(t)) = \eta \left[y^{*''}(s(t)) \dot{s}^2(t) + y^{*'}(s(t)) \ddot{s}(t) + \alpha y^{*'}(s(t)) \dot{s}(t) + \alpha \beta (y^*(s(t)) - g_r) \right]. \quad (15)$$

By distributing the scaling factor η across all the terms on the right side of (15), one can express $f(s(t))$ as a linear combination of

$$y_{\eta}^*(s) = \eta y^*(s) \quad (16)$$

and its derivatives.

The complete schematic view of the Transformation System with the forcing term (15) is reported in Fig. 1. Note that it enables the following features [20], [35]: time modulation by varying the evolution of the phase $s(t)$; phase reversibility allowing forward and backward reproduction of the trajectory, when $\dot{s}(t) > 0$ and $\dot{s}(t) < 0$, respectively; spatial modulation of the curve varying the initial position $y(s(0))$ and the goal g of the task.

The TS can then be generalized to the multidimensional case. In the proposed experimental application, described in Sec. V, only the robot position is considered. Therefore, the expression of the TS in the Cartesian space is used, i.e.

$$\ddot{\mathbf{y}}(t) + \mathbf{A}\dot{\mathbf{y}}(t) + \mathbf{A}\mathbf{B}(\mathbf{y}(t) - \mathbf{g}) = \mathbf{E}\mathbf{f}^*(s(t)), \quad (17)$$

where $\mathbf{A} = \text{diag}(\alpha_x, \alpha_y, \alpha_z)$, $\mathbf{B} = \text{diag}(\beta_x, \beta_y, \beta_z)$, $\mathbf{E} = \text{diag}(\eta_x, \eta_y, \eta_z)$, and

$$\mathbf{y}(t) = \begin{bmatrix} y_x(t) \\ y_y(t) \\ y_z(t) \end{bmatrix}, \quad \mathbf{g} = \begin{bmatrix} g_x \\ g_y \\ g_z \end{bmatrix}, \quad \mathbf{f}^*(s) = \begin{bmatrix} f_x^*(s(t)) \\ f_y^*(s(t)) \\ f_z^*(s(t)) \end{bmatrix}. \quad (18)$$

Note that equations (17)-(18) can also be generalized to consider the end-effector (EE) orientation [14], [36].

A. Spatial Sampling Algorithm

A wide variety of applications utilize DMP as a core for a Learning by Demonstration (LbD) framework to effectively reproduce the reference trajectories in both space and time [7], [14]. In particular, one can set the Canonical System (CS) in (3) to ensure that the output of the DMP accurately reproduces the reference trajectory, including its time dependency [15]. This means that, if the user stops while recording the reference trajectory, this information will also be included in the parameterization of the desired trajectory. In the classical formulation of DMP, the duration of this pausing phase can be shortened or extended by appropriately adjusting parameter τ in (1)-(3). However, it will persist while reproducing the desired trajectory, [41]. Also the formulation reported in Fig. 1, does not eliminate this side effect, since a stop in the demonstrated trajectory involves $\mathbf{y}^{*\prime}(s) = \mathbf{y}^{*\prime\prime}(s) = 0$ and consequently, from (14), $\dot{\mathbf{y}}^*(s(t)) = \ddot{\mathbf{y}}^*(s(t)) = 0$ regardless of the chosen phase variable $s(t)$.

This issue becomes especially significant in applications where recording solely the traveled space is necessary, i.e., encoding a desired path irrespective of velocity and acceleration profiles.

In [20], the reference trajectory is recorded in two steps by teaching the path and the velocity profiles separately. Another example of an application based on the demonstrated geometric path can be found in [28]. In this work, the authors introduce a varying scaling factor of the time in the DMP formulation, modulated by the tangent component of an external force. However, when the velocity along the curve slows down to zero during the demonstration, the tangent vector to the curve tends to zero as well. In instances where the velocity during the demonstration is exactly zero, the tangent direction is undefined, requiring special treatment in such cases. To fix the above-mentioned issues, we propose to parameterize the forcing term $f^*(s)$ starting from an expression of the learned trajectory, which is a function of a curvilinear abscissa, i.e., the length along the curve, rather than time. This can be achieved by considering a novel sampling algorithm for the sequence of demonstrated positions, named "spatial sampling", that records the points when they are at a prescribed distance Δ .

The proposed procedure, whose Matlab code ¹ is reported in App. B-Fig. 18, is based on two steps:

- 1) Starting from the sequence of samples obtained by recording the demonstrated trajectory $\mathbf{y}_r(t) = [y_{r_x}(t), y_{r_y}(t), y_{r_z}(t)]^T$ with constant period T ,

$$\mathbf{y}_{T,k} = \mathbf{y}_r(t_k) = \mathbf{y}_r(kT) \quad k = 0, \dots, N,$$

a continuous-time function $\mathbf{y}_L(t)$ is built by applying a First-Order Hold (FOH) on it [44]. In this way, the function $\mathbf{y}_L(t)$ linearly interpolates the samples

obtained from $\mathbf{y}_r(t)$, and if the sampling period T is small enough one can assume that $\mathbf{y}_L(t) \simeq \mathbf{y}_r(t)$.

- 2) In the second step of this procedure, a new sequence $\mathbf{y}_{\Delta,k}$ is obtained by imposing that $\mathbf{y}_{\Delta,0} = \mathbf{y}_L(0)$ and then, for $k > 0$, $\mathbf{y}_{\Delta,k} = \mathbf{y}_L(t_{\Delta,k})$, where $t_{\Delta,k}$ is the time value that guarantees

$$\|\mathbf{y}_{\Delta,k} - \mathbf{y}_{\Delta,k-1}\| = \Delta, \quad \text{for } k = 1, \dots, M. \quad (19)$$

The free parameter Δ defines the geometric distance between consecutive samples.

Because of the condition (19), the total distance between the first point $\mathbf{y}_{\Delta,0}$ and the generic k -th point $\mathbf{y}_{\Delta,k}$, $k > 0$, is simply given by $k\Delta$. This distance approximates the length of the curve $\mathbf{y}_L(t)$ at the time instant $t_{\Delta,k}$, with a precision that depends on the value of Δ . Therefore, for Δ small enough, the new sampling mechanism induces a mapping between the length $s_k = k\Delta$ and the position along the approximating linear curve \mathbf{y}_L , i.e.

$$\mathbf{y}_{\Delta,k} = \mathbf{y}_L(t_{\Delta,k}) \quad \text{with } t_{\Delta,k} = \gamma^{-1}(s_k) \quad (20)$$

where $s = \gamma(t)$ is the particular timing law imposed during the demonstration of the trajectory which describes how the robot moves along the imposed geometric path, being variable s the arc-length parameterization of the curve. In conclusion, given the analytical expression of the trajectory parameterized with respect to the curvilinear abscissa $\hat{\mathbf{y}}_r(s) \approx \hat{\mathbf{y}}_L(s) = \mathbf{y}_L(\gamma^{-1}(s))$, the sequence $\mathbf{y}_{\Delta,k}$ can be viewed as the result of a sampling operation with a constant spatial period Δ . Interestingly,

$$\left\| \frac{d\hat{\mathbf{y}}_r(s)}{ds} \right\|_{s=s_k} \approx \frac{\|\mathbf{y}_{\Delta,k+1} - \mathbf{y}_{\Delta,k}\|}{\|s_{k+1} - s_k\|} = \frac{\Delta}{\Delta} = 1. \quad (21)$$

Consequently, this derivative will always be different from zero, and the tangent direction will always be well-defined. The operation of the algorithm is graphically depicted in Fig. 2 for a one-dimensional case study. Initially, by sampling the reference trajectory $y_L(t_T)$ at a constant time interval T , we derive the linear interpolation function $y_L(t)$. The geometric distance Δ_k between adjacent points is obviously varying. Subsequently, in Fig. 2b and Fig. 2c, the curve $y_L(t)$ is re-sampled using two different spatial intervals Δ . It is evident that smaller values of Δ result in a more accurate approximation of the original curve. In Fig. 2d, the samples of the timing-law $s = \gamma(t)$ imposed during the demonstration of the trajectory and obtained with the same spatial period Δ of case (c) are also presented. These illustrate how the length along the geometric path changes with time throughout the demonstration.

Remark 1: The diagram depicted in Fig. 1, where the parametric function $\mathbf{y}^*(s)$ is computed based on the pair $(s_k, \mathbf{y}_{\Delta,k})$, $k = 0, \dots, M$, defines the *Geometric DMP* (GDMP). This type of DMP solely derives from the geometric path of the demonstrated trajectory and can be linked to any phase variable $s(t)$.

V. APPLICATIONS OF GEOMETRIC DMP

In this section, we illustrate some applications that can benefit from the new concept of Geometric DMP.

¹All codes are publicly available at the following repository: <https://github.com/giobraglia/Geometric-Dynamic-Motion-Primitives.git>

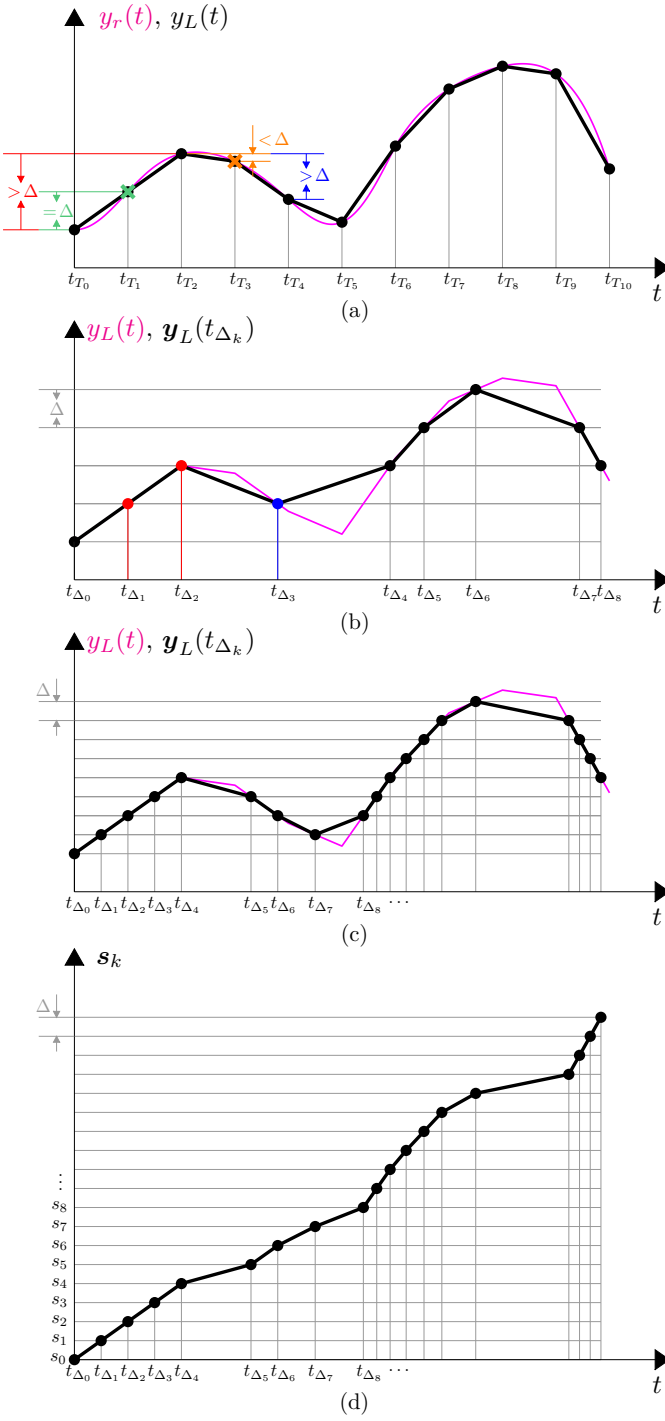


Figure 2: Sketch displaying the operation of the Spatial Sampling algorithm in a one-dimensional scenario: reference trajectory $y_L(t)$ sampled with constant period T and interpolating linear curve $y_L(t)$ (a), sequence of spatially sampled points $y_{L,k} = y_L(t_{\Delta_k})$ with $\Delta = \bar{\Delta}$ (b) and $\Delta = \bar{\Delta}/2$ (c), and samples of the function $s_k = \gamma(t_{\Delta_k})$ for $\Delta = \bar{\Delta}/2$ (d).

Considering that DMP-based methods aim at reproducing a given reference motion, typically defined via a teaching-by-demonstration technique, the decoupling between the Transformation System and the phase variable $s(t)$, which

can be freely chosen, leads to three distinct scenarios, depicted in Fig. 3:

- 1) The given trajectory is replicated precisely as demonstrated.
- 2) The motion along the geometric path encoded by the DMP is optimized to achieve secondary objectives, such as minimizing the execution time while ensuring compliance with task-imposed constraints or the physical limits of the robotic system.
- 3) Similar to the standard DMP definition, the phase variable $s(t)$ is defined by a dynamical system, possibly dependent on external inputs. For instance, in a co-manipulation task, $s(t)$ might be generated based on the force exerted by a human on a robot manipulator.

While in case (1) it is sufficient to consider $s(t) = \gamma(t)$, in case (2) it is necessary to set up and solve an optimization problem, as detailed in Sec. V-A. Finally, in case (3), which is the main focus of this paper, the definition of $s(t)$ involving a human in the loop necessitates a passivity analysis and a proper modification of the basic DMP formulation to ensure the overall stability of the robotic system. These aspects will be thoroughly addressed in Sec. VI- VII.

A. Phase Optimization in Geometric DMP

The basic use of GDMP involves minimizing the duration of the motion under task and kinematic constraints [32], [39], [45], [46]. For example, an optimization problem employing the standard DMP was addressed in [35]. A quadratic cost function was introduced to determine the DMP trajectory that meets the robot's kinematic constraints while closely approximating the reference trajectory. In that paper, the authors optimize the set of weights ω parameterizing the reference position trajectories. In our work, we directly optimize the phase variable $s(t)$, which is considered the output of a second-order system, namely a chain of two integrators:

$$\dot{\mathbf{x}} = \begin{bmatrix} 0 & 1 & 0 \\ 0 & 0 & 1 \\ 0 & 0 & 0 \end{bmatrix} \mathbf{x} + \begin{bmatrix} 0 \\ 0 \\ 1 \end{bmatrix} u,$$

where $\mathbf{x} = [s(t), \dot{s}(t), \ddot{s}(t)]^T$ and $u = \ddot{s}(t)$ [12]. The optimization problem can be formulated as follows [46]:

$$\min_{u(\cdot)} T_f = \int_0^{T_f} 1 dt = \int_0^{\Delta M} \frac{1}{\dot{s}} ds,$$

subject to:

$$\begin{aligned} s(0) &= 0, & s(T_f) &= \Delta M, \\ \dot{s}(0) &= \dot{s}(T_f) = 0, & \dot{s} &\geq 0, \\ \ddot{s}(0) &= \ddot{s}(T_f) = 0. \end{aligned}$$

Additionally, there are conditions directly imposed on \mathbf{x} and u :

$$\begin{aligned} |\dot{s}(t)| &\leq \dot{s}_{\text{MAX}}, \\ |\ddot{s}(t)| &\leq \ddot{s}_{\text{MAX}}, \\ |\ddot{\ddot{s}}(t)| &\leq \ddot{\ddot{s}}_{\text{MAX}}, \end{aligned} \quad (22)$$

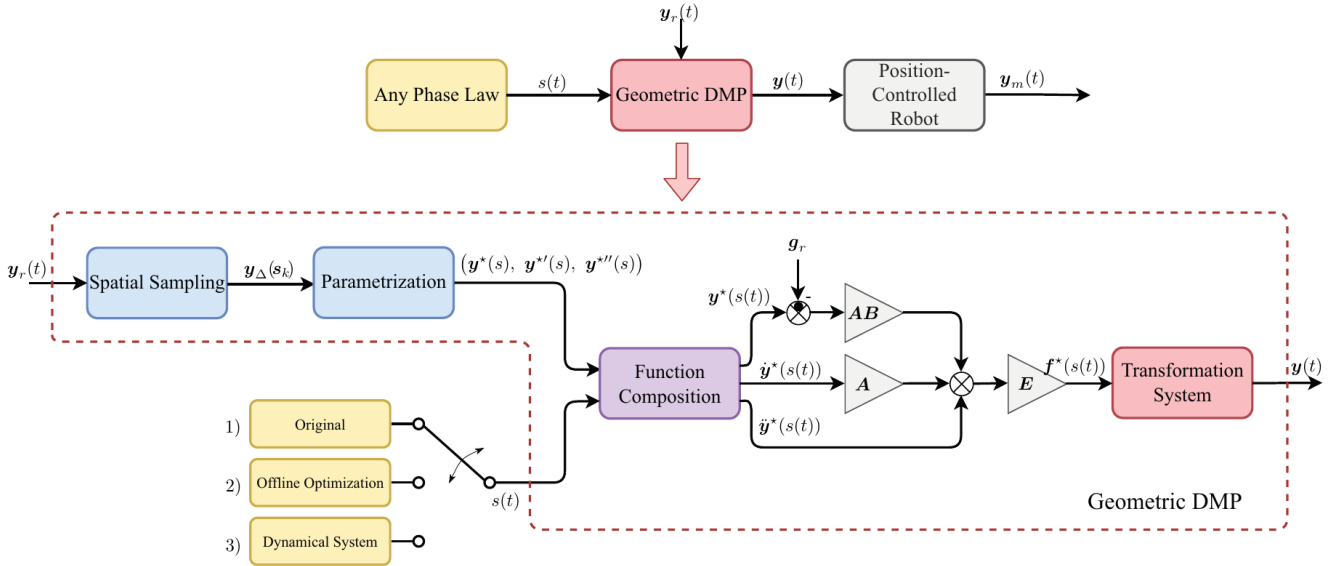


Figure 3: Schematic of the proposed framework based on Geometric DMP.

or in the robot task space,

$$\begin{aligned} \|\eta \dot{\mathbf{y}}^*(s(t))\| \leq \dot{\mathbf{y}}_{\text{MAX}} &\Leftrightarrow \|\dot{\mathbf{y}}^*(s(t))\| \leq \dot{\mathbf{y}}_{\text{MAX}}/\eta, \\ \|\eta \ddot{\mathbf{y}}^*(s(t))\| \leq \ddot{\mathbf{y}}_{\text{MAX}} &\Leftrightarrow \|\ddot{\mathbf{y}}^*(s(t))\| \leq \ddot{\mathbf{y}}_{\text{MAX}}/\eta, \end{aligned} \quad (23)$$

where the geometric scaling factor η has also been considered. By exploiting the relationships (14), conditions (23) can be translated into constraints on $\dot{s}(t)$, $\ddot{s}(t)$, etc. In particular, since $\|\mathbf{y}'(s(t))\| = 1$ by construction, the condition on the velocity in (22) and (23) are equivalent, i.e.

$$\|\dot{\mathbf{y}}^*(s(t))\| \leq \dot{\mathbf{y}}_{\text{MAX}}/\eta \Leftrightarrow |\dot{s}(t)| \leq \dot{s}_{\text{MAX}} = \dot{\mathbf{y}}_{\text{MAX}}/\eta.$$

Alternatively, or in addition, one can consider constraints in the joint space of the robot manipulator, typically caused by the physical limitations of the actuation systems. For an n -Degree-Of-Freedom (DOF) robot, if $\mathbf{q}^*(s) \in \mathbb{R}^n$ represents the joint trajectory profiles corresponding to the task space motion $\mathbf{y}_\eta^*(s)$, i.e.

$$\mathbf{q}^*(s) = \text{IK}(\mathbf{y}_\eta^*(s)),$$

where $\text{IK}(\cdot)$ denotes the Inverse Kinematics function of the robot, the constraints can be expressed as:

$$\begin{aligned} |\dot{\mathbf{q}}^*(s(t))| &\leq \dot{\mathbf{q}}_{\text{MAX}}, \\ |\ddot{\mathbf{q}}^*(s(t))| &\leq \ddot{\mathbf{q}}_{\text{MAX}}. \end{aligned} \quad (24)$$

These constraints account for the velocity and acceleration limits in the joint space of the robot manipulator. Moreover, even if the optimization is performed offline, it is necessary to consider the scaling factor η , which depends on the actual initial position and the goal.

To demonstrate the efficacy of the phase-variable definition based on an optimization problem using the GDMP, we implemented the aforementioned method on the curve depicted in Fig. 4 obtained by kinesthetic teaching on the Franka Emika Panda robot. Specifically, the constraints

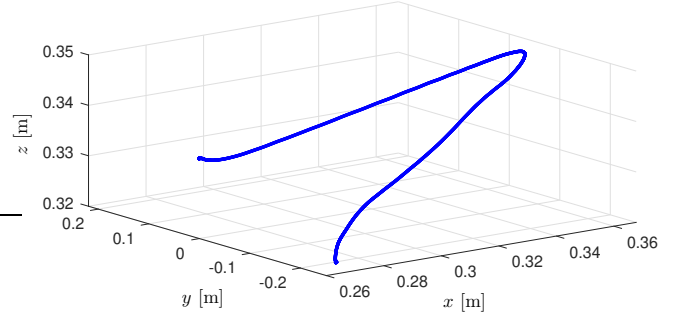


Figure 4: Demonstrated curve used in the optimization problem.

(22) were initially taken into account. Subsequently, in another experiment following the same geometric path, the bounds (24), meeting the specifications provided by the robot manufacturer [47], were considered.

The numerical results, obtained using the CasADi optimal solver [48] within the MATLAB environment, are reported in Fig. 5. This figure compares the phase variable $s(t)$ obtained in the two cases, namely $\gamma_s(t)$ and $\gamma_q(t)$, with the original timing-law $\gamma(t)$. Furthermore, the outcome of a third minimization problem, incorporating both conditions (22) and (24), is also presented. Upon analyzing Fig. 5, it is apparent that the optimization of the phase variable $s(t)$, under the numerical bounds applied in the experiments, significantly reduces the motion duration compared to the demonstrated trajectory lasting 3.1 seconds: $\gamma_s(t)$ spans a duration of 1.1 seconds (with a reduction of -64.5%), while $\gamma_q(t)$ lasts 0.6 seconds (-80.6%). It is worth noting that when both constraints are considered, the duration of $\gamma_{qs}(t)$ remains the same as $\gamma_s(t)$, indicating that the bounds directly applied to the derivatives of $s(t)$ are more restrictive than the limits at the joints level. The derivatives' profiles of $\gamma_s(t)$, displayed

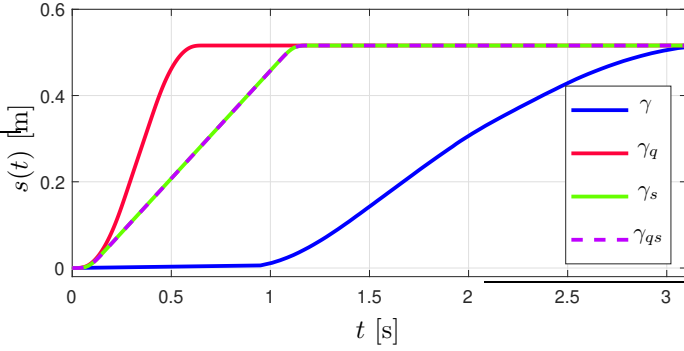


Figure 5: Phase profiles obtained as a solution of the optimization problem with conditions (22) and (24).

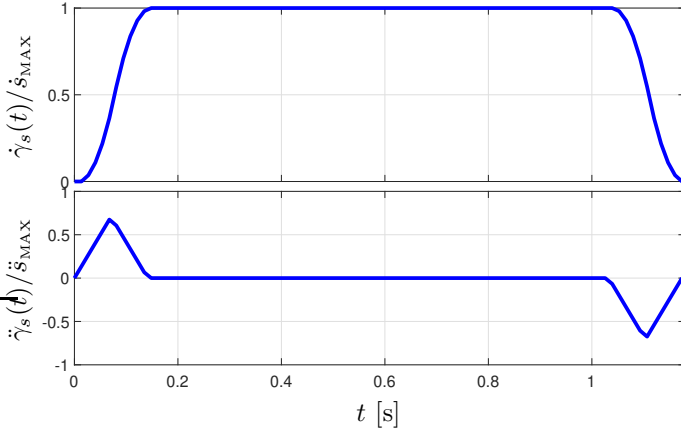


Figure 6: Derivatives of the optimal phase profile $\gamma_s(t)$ minimizing the duration of the trajectory under the constraints (22).

in Fig. 6, confirm the optimality of the function within the given constraints over time. This is evident as, at every time instant, at least one constraint is satisfied. Similar conclusions can be drawn for $\gamma_q(t)$ by referring to Fig. 7, which presents joint velocity and acceleration profiles. Here, the limiting factors are the velocity of joint #7 and the acceleration of joint #3.

As mentioned above, the optimization of the phase profile $s(t)$ is conducted offline using the reference trajectory $\mathbf{y}^*(s)$. In theory, this optimization could be performed online by incorporating the real-time state of the TS. However, this particular issue is beyond the scope of this document. To provide an example of online $s(t)$ phase signal generation, a second-order system driven by the force applied by a human operator is instead considered, as detailed in the next section.

VI. HUMAN-IN-THE-LOOP GEOMETRIC DMP

In this scenario, illustrated schematically in Fig. 8, the phase variable $s(t)$ is determined by a second-order differential equation:

$$m \ddot{s}(t) + b \dot{s}(t) = \mathbf{y}^{*'}(s(t))^T \mathbf{E} \mathbf{F}_h(t). \quad (25)$$

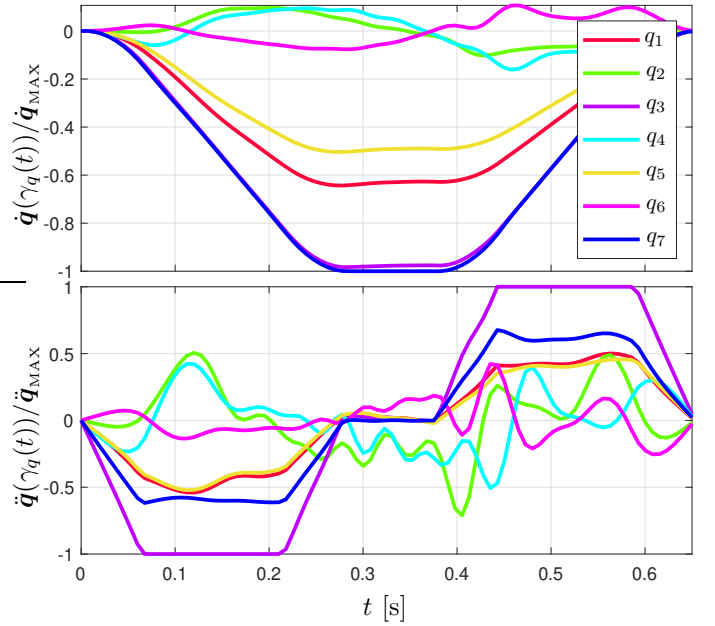


Figure 7: Normalized joint velocities and accelerations obtained with the phase profile $\gamma_q(t)$, optimizing the trajectory duration under joint constraints.

This equation represents the dynamics of a mass m with damping b , influenced by the external force $\mathbf{F}_h(t)$ applied to the robot end-effector by a human operator, measured using an appropriate sensor. The presence of the scaling factor \mathbf{E} in (25) is necessary for two reasons:

- It facilitates intuitive interaction between the user and this virtual physical system.
- It ensures the stability of the feedback system from a formal standpoint.

Given that $\mathbf{E}^T = \mathbf{E}$ is a diagonal matrix, the expression $\mathbf{y}^{*'}(s)^T \mathbf{E} = (\mathbf{E} \mathbf{y}^{*'}(s))^T$ can be interpreted as the transposed derivative with respect to s of the curve $\mathbf{y}_\eta^*(s) = \mathbf{E} \mathbf{y}^*(s)$. This curve extends the scaled function (16) into a multi-dimensional space. Consequently, (25) can be reformulated as:

$$m \ddot{s}(t) + b \dot{s}(t) = \mathbf{y}_\eta^{*'}(s(t))^T \mathbf{F}_h(t). \quad (26)$$

The cross-product $\mathbf{y}_\eta^{*'}(s(t))^T \mathbf{F}_h(t)$ denotes the projection of the human force vector $\mathbf{F}_h(t)$ onto the tangent direction of the reference trajectory $\mathbf{y}_\eta^*(s(t))$. This trajectory, aside from the scaling factor \mathbf{E} , is parameterized by the spatially-sampled reference trajectory $\mathbf{y}_\Delta(s)$ in (20). According to (21), $\|\mathbf{y}^{*'}(s(t))\| = 1$, and hence $\|\mathbf{y}_\eta^{*'}(s(t))\| = \text{const} \neq 0$. This means that the projection in (26) can always be successfully computed [11], [12], [49]. Note that this presents an alternative solution to the approach proposed in [28], where preventing the tangent component computed from the reference velocity trajectory from approaching zero is achieved by introducing a minimum threshold instead. In conclusion, only the component of the force $\mathbf{F}_h(t)$ tangent to the reference

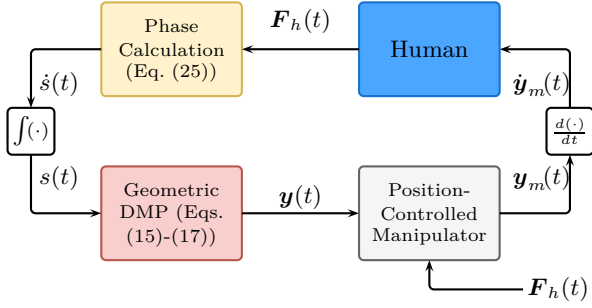


Figure 8: Human-robot interaction through kinesthetic guidance along the trajectories encoded by a GDMP.

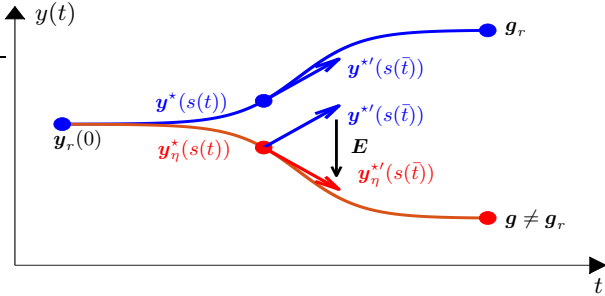


Figure 9: An example showcasing the impact of the scaling matrix \mathbf{E} in (25) on the projection of the force $\mathbf{F}_h(t)$.

trajectory encoded by the GDMP influences the dynamics of the phase variable $s(t)$.

Considering the role of $\mathbf{y}_\eta^{*'}(s(t))$ in (26), the purpose of the scaling matrix \mathbf{E} becomes clearer through a simple qualitative 1-D example depicted in Fig. 9. The figure compares the reference trajectory encoded by the GDMP, $\mathbf{y}^*(s(t))$ (blue), with the trajectory $\mathbf{y}_\eta^{*'}(s(t))$ (red) generated under nominal conditions by the GDMP when a new goal position $\mathbf{g} \neq \mathbf{g}_r$ is chosen. The inclusion of matrix \mathbf{E} ensures that the tangent direction remains consistent with the current orientation of the new curve. This feature proves valuable as it guarantees an accurate projection of the force $\mathbf{F}_h(t)$ in (26) without the necessity of a new DMP parameterization [23], [36].

After numerically solving (26) to determine $s(t)$, the latter is then employed in a slightly modified version of the GDMP described by:

$$\ddot{\mathbf{y}}(t) + \mathbf{A}\dot{\mathbf{y}}(t) + \mathbf{A}\mathbf{B}\mathbf{y}(t) - \mathbf{A}\mathbf{B}\mathbf{g} =$$

$$\mathbf{E}[\dot{\mathbf{y}}^*(s(t)) + \mathbf{A}\dot{\mathbf{y}}^*(s(t)) + \mathbf{A}\mathbf{B}\mathbf{y}^*(s(t)) - \mathbf{A}\mathbf{B}\mathbf{g}_r] + \mathbf{F}_h(t), \quad (27)$$

where the additional term $\mathbf{F}_h(t)$ is introduced to ensure the stability of the feedback system, as demonstrated in Sec. VI-A. It is essential to note that if the parameters \mathbf{A} and \mathbf{B} are sufficiently large, it becomes feasible to limit the deviation between the actual DMP trajectory $\mathbf{y}(t)$ and the nominal trajectory $\mathbf{y}^*(s(t))$ below a specified tolerance.

The motion trajectory $\mathbf{y}(t)$ is then fed into a robot manipulator equipped with high-gain position control. This control system is expected to ensure precise tracking of the reference trajectory, i.e. $\mathbf{y}_m(t) \approx \mathbf{y}(t) \forall t$, despite the force exerted on the manipulator by the human user.

The proposed scheme essentially implements an admittance control system for physical interaction with the human operator [50]. In this setup, the admittance model restricts the user's movement to follow the trajectories defined by the GDMP, allowing forward or backward motion. Given the feedback structure of the overall control system, ensuring stability in the dynamics involving the Human, GDMP, and robot manipulator becomes essential. As suggested in [50], although the human user might demonstrate non-passive dynamic behavior, a feasible approach for ensuring stability in human-robot interaction involves enforcing an energetically passive behavior of the apparent dynamics of the controlled robot. Therefore, the examination will focus on the system's passivity at the power port with the human, specifically $\langle \dot{\mathbf{y}}_m, \mathbf{F}_h \rangle$.

A. Passivity Analysis

Definition 1: Let $P_T(t) = \sum_{i=1}^n P_i(t) = \mathbf{u}^T(t)\mathbf{z}(t)$ be the total power flowing through the n energetic ports of a dynamical system, where $\mathbf{u}(t)$ and $\mathbf{z}(t)$ are the input and output vectors [51]. Such a system is said to be passive if there exists a non-negative storage function $S(\mathbf{x}(t))$ of the state vector $\mathbf{x}(t)$ such that, for any time interval $[t_0, t_1]$ and for any initial state vector \mathbf{x}_0 and being \mathbf{x}_1 the state vector at time t_1 , it holds [52], [53]:

$$S(\mathbf{x}_1) - S(\mathbf{x}_0) \leq \int_{t_0}^{t_1} P_T(t) dt. \quad (28)$$

Note that (28) is equivalent to

$$\dot{S}(\mathbf{x}(t)) \leq P_T(t). \quad (29)$$

Property 1: The system in Fig. 8, describing the human-robot interaction through kinesthetic guidance, is passive with respect to the energetic port $P_T = \dot{\mathbf{y}}_m^T(t)\mathbf{F}_h(t)$, being $\dot{\mathbf{y}}_m(t)$ the actual manipulator velocity. *Proof.*

Let variables $\tilde{\mathbf{y}}$, $\dot{\tilde{\mathbf{y}}}$ and $\ddot{\tilde{\mathbf{y}}}$ be defined as:

$$\tilde{\mathbf{y}}(t) = \mathbf{y}(t) - \mathbf{g} - \mathbf{E}\mathbf{y}^*(s(t)) + \mathbf{E}\mathbf{g}_r,$$

$$\dot{\tilde{\mathbf{y}}}(t) = \frac{d\tilde{\mathbf{y}}(t)}{dt} = \dot{\mathbf{y}}(t) - \mathbf{E}\dot{\mathbf{y}}^*(s(t)), \quad (30)$$

$$\ddot{\tilde{\mathbf{y}}}(t) = \frac{d\dot{\tilde{\mathbf{y}}}(t)}{dt} = \ddot{\mathbf{y}}(t) - \mathbf{E}\ddot{\mathbf{y}}^*(s(t)),$$

where \mathbf{g} and \mathbf{g}_r are the goals of the desired and parameterized demonstrated trajectories $\mathbf{y}(t)$ and $\mathbf{y}^*(s(t))$, respectively. Using (30), Eq. (27) can be rewritten as the following second-order matrix differential equation:

$$\ddot{\tilde{\mathbf{y}}}(t) + \mathbf{A}\dot{\tilde{\mathbf{y}}}(t) + \mathbf{A}\mathbf{B}\tilde{\mathbf{y}}(t) = \mathbf{F}_h(t), \quad (31)$$

representing the dynamics of a mass-spring-damper system with unitary mass, damping \mathbf{A} and stiffness $\mathbf{A}\mathbf{B}$, in the three-dimensional space. The following storage function $S(\tilde{\mathbf{y}}(t), \dot{\tilde{\mathbf{y}}}(t))$ for the system in (31) and (25) can be considered:

$$S(\tilde{\mathbf{y}}(t), \dot{\tilde{\mathbf{y}}}(t)) = \underbrace{\frac{1}{2}\dot{\tilde{\mathbf{y}}}^T(t)\dot{\tilde{\mathbf{y}}}(t)}_{E_{K_1}} + \underbrace{\frac{1}{2}\tilde{\mathbf{y}}^T(t)\mathbf{A}\mathbf{B}\tilde{\mathbf{y}}(t)}_{E_U} + \underbrace{\frac{1}{2}m\dot{s}^2(t)}_{E_{K_2}}, \quad (32)$$

where E_{K_1} and E_U represent the kinetic and potential energies respectively stored in the GDMP dynamics (15)-(17), see the red block in Fig. 8, while E_{K_2} is the kinetic energy of the mass-damper dynamics (25) responsible for the generation of the phase variable $s(t)$ based on the human force, see the yellow block in Fig. 8. By differentiating the storage function $S(\tilde{\mathbf{y}}(t), \dot{\tilde{\mathbf{y}}}(t))$ in (32) with respect to time, the resulting function becomes:

$$\dot{S}(t) = \dot{\tilde{\mathbf{y}}}^T(t) [\ddot{\tilde{\mathbf{y}}}(t) + \mathbf{A}\mathbf{B}\tilde{\mathbf{y}}(t)] + m\dot{s}(t)\ddot{s}(t).$$

Substituting $\ddot{\tilde{\mathbf{y}}}(t)$ from (31), one obtains:

$$\begin{aligned} \dot{S}(t) = & \dot{\tilde{\mathbf{y}}}^T(t) [-\mathbf{A}\dot{\tilde{\mathbf{y}}}(t) - \mathbf{A}\mathbf{B}\tilde{\mathbf{y}}(t) + \mathbf{F}_h(t) + \mathbf{A}\mathbf{B}\tilde{\mathbf{y}}(t)] + \\ & + m\dot{s}(t)\ddot{s}(t). \end{aligned}$$

Further substitution of $\ddot{s}(t)$ from (25) yields:

$$\begin{aligned} \dot{S}(t) = & -\dot{\tilde{\mathbf{y}}}^T(t)\mathbf{A}\dot{\tilde{\mathbf{y}}}(t) + \dot{\tilde{\mathbf{y}}}^T(t)\mathbf{F}_h(t) + \\ & - b\dot{s}^2(t) + \dot{s}(t)\mathbf{y}^{*T}(s(t))\mathbf{E}\mathbf{F}_h(t). \end{aligned}$$

Finally, substituting $\dot{\tilde{\mathbf{y}}}(t)$ in (30) and recalling that $\mathbf{y}^{*T}(s(t))\dot{s}(t) = \dot{\mathbf{y}}^{*T}(s(t))$ from (14), the expression becomes:

$$\begin{aligned} \dot{S}(t) = & -\dot{\tilde{\mathbf{y}}}^T(t)\mathbf{A}\dot{\tilde{\mathbf{y}}}(t) + [\dot{\mathbf{y}}(t) - \mathbf{E}\dot{\mathbf{y}}^{*T}(s(t))]^T \mathbf{F}_h(t) + \\ & - b\dot{s}^2(t) + \dot{\mathbf{y}}^{*T}(s(t))\mathbf{E}\mathbf{F}_h(t) \quad (33) \\ = & -\dot{\tilde{\mathbf{y}}}^T(t)\mathbf{A}\dot{\tilde{\mathbf{y}}}(t) + \dot{\mathbf{y}}^T(t)\mathbf{F}_h(t) - b\dot{s}^2(t). \end{aligned}$$

Considering the energetic port $P_T = \dot{\mathbf{y}}_m^T(t)\mathbf{F}_h(t)$, and utilizing (33), condition (29) becomes evidently fulfilled. Indeed, assuming perfect tracking by the robot of the reference trajectory generated by the DMP, i.e. $\mathbf{y}_m(t) = \mathbf{y}(t)$ and consequently $\dot{\mathbf{y}}_m(t) = \dot{\mathbf{y}}(t)$, the inequality

$$-\dot{\tilde{\mathbf{y}}}^T(t)\mathbf{A}\dot{\tilde{\mathbf{y}}}(t) + \dot{\mathbf{y}}^T(t)\mathbf{F}_h(t) - b\dot{s}^2(t) \leq \dot{\mathbf{y}}_m^T(t)\mathbf{F}_h(t), \quad (34)$$

transforms into

$$-\dot{\tilde{\mathbf{y}}}^T(t)\mathbf{A}\dot{\tilde{\mathbf{y}}}(t) - b\dot{s}^2(t) \leq 0 \quad (35)$$

which is always satisfied for $\mathbf{A} > 0$ and $b > 0$.

VII. EXPERIMENTS AND EVALUATION

This section presents and discusses experimental tests conducted to validate the proposed framework. Section VII-A outlines the utilized setup and details the performed experimental tests. The selection of parameters m and b in (25), which significantly influence the human-robot interaction, is treated in Section VII-B. Finally, a comprehensive discussion of the experimental outcomes is provided in Section VII-C.

A. Experimental Setup

The experimental setup is based on a Franka Emika Panda robot. Various tests were conducted to implement the Geometric DMP (GDMP) architecture depicted in Fig. 8 in the context of co-manipulation tasks emulating upper-limb rehabilitation operations. Three distinct experimental tests, illustrated in Fig. 10, were designed,

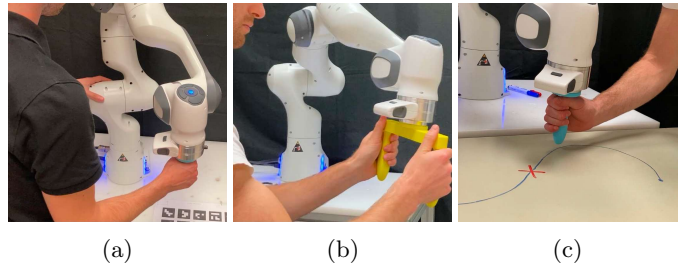


Figure 10: Snapshots of experimental tests: (a) Internal/External rotation of the shoulder, (b) Bi-manual grabbing, (c) Stop at a point.

requiring the user to manipulate the robot's End-Effector (EE) along the desired position trajectory $\mathbf{y}(t)$ generated by the GDMP. The position of the EE is controlled through a joint velocity regulator developed in the MATLAB/Simulink environment. From Fig. 10, one can appreciate the two custom EEs which have been 3D-printed. The EE in Fig. 10a and Fig. 10c is composed of one handle as the considered exercise requires the user to move one arm only. The EE in Fig. 10b consists of two handles as the considered exercise requires the user to move two arms. In the first test, see Fig. 10a (minute 0:27 in the video ²), the user is required to perform an internal and external rotation of the shoulder in the upright position. The second task in Fig. 10b (minute 0:51) requires the user to lead the EE from the initial to the goal position using a bi-manual grabbing in a seated position. Finally, in the third experiment shown in Fig. 10c (minute 1:19), the user is required to move the EE from the initial position to a given point located along the demonstrated trajectory. For each task, an expert user demonstrated the reference position trajectory $\mathbf{y}_r(t)$ through kinesthetic guidance. The Spatial Sampling algorithm, outlined in Fig. 18, was then employed on $\mathbf{y}_r(t)$ to produce a sequence of samples $\mathbf{y}_{\Delta,k}$ spaced at distance Δ . Subsequently, these points were interpolated to derive the parameterized position trajectory $\mathbf{y}^*(s(t))$ dependent on the arc-length.

The experiments displayed in Fig.10 involved several participants of varying genders, aged between 20 and 60, out of whom only three possessed prior expertise in robotics.

B. Parameters Tuning

In the implementation of GDMP outlined in Fig. 3 and Fig. 8, the parameters $\alpha_x = \alpha_y = \alpha_z = 40$ and $\beta_x = \beta_y = \beta_z = 10$ were assigned to the matrices \mathbf{A} and \mathbf{B} in (17). This ensures a sufficiently high stiffness value for the equivalent second-order system in (31), which models the dynamics of the GDMP, and, even in the presence of the additional external force $\mathbf{F}_h(t)$, contributes to maintaining a small deviation of the output with respect to the desired position trajectory, i.e., $\mathbf{y}(t) \approx \mathbf{y}^*(s(t))$.

While the selection of the elements within matrices \mathbf{A} and \mathbf{B} is not particularly critical, the choice of m and b

²The video can be found at: <https://youtu.be/1wy9qlHA66o>

in the phase filter (25) becomes pivotal in practical applications, despite the stability proof reported in Sec. VI-A. In this case, first-attempt values could be deduced from the physical limitations of the Franka Emika Panda robot. Specifically, the numerical values for the maximum Cartesian velocity and acceleration are $\dot{\mathbf{y}}_{\text{MAX}} = 1.7$ m/s and $\ddot{\mathbf{y}}_{\text{MAX}} = 13.0$ m/s², respectively [47]. Since the payload of the robot is 3 kg, this implies that the force limit is $F_{\text{MAX}} = 30N$.

With the proposed parameterization of the demonstrated trajectory and under the nominal condition where $\mathbf{E} = \mathbf{I}_3$, $\|\dot{\mathbf{y}}^*(s(t))\| = |\dot{s}(t)|$, and if the curvature is negligible, $\|\ddot{\mathbf{y}}^*(s(t))\| \approx |\ddot{s}(t)|$. Consequently,

$$\dot{s}_{\text{MAX}} = 1.7 \text{ m/s} \quad \text{and} \quad \ddot{s}_{\text{MAX}} = 13.0 \text{ m/s}^2.$$

Let us consider Eq. (25) describing the dynamics of the phase variable $s(t)$, rewritten as:

$$m\ddot{s}(t) + b\dot{s}(t) = F_\tau(t) \quad (36)$$

where, for $\mathbf{E} = \mathbf{I}_3$, $F_\tau(t) = \mathbf{y}^{*'}(s(t))^T \mathbf{F}_h(t)$ denotes the tangent force. When the user accelerates the mass from zero velocity and causes a peak of acceleration, the instantaneous relation simplifies to:

$$m\ddot{s}(t) = F_\tau(t) \quad (37)$$

While under steady-state conditions (when $\ddot{s}(t) = 0$ and the peak velocity occurs), it leads to:

$$b\dot{s}(t) = F_\tau(t) \quad (38)$$

Therefore, the values of m and b can be determined as:

$$m = \frac{F_{\text{MAX}}}{\ddot{s}_{\text{MAX}}} \approx 2 \text{ kg} \quad \text{and} \quad b = \frac{F_{\text{MAX}}}{\dot{s}_{\text{MAX}}} \approx 17 \text{ N s/m}. \quad (39)$$

While the values in (39) ensure the motion's feasibility under various conditions, additional considerations are influencing the selection of these parameters. Particularly in a rehabilitation task, it is expected that the force exerted by the user remains considerably smaller than F_{MAX} . Ideally, in applications where the users must move freely along trajectories encoded by the DMP, the forces experienced in the tangent direction to the curve should be minimized. As a result, parameters m and b should be chosen to be very small. Hence, in the experimental phase, instead of a singular value for m and b , we consider an acceptable range, specifically:

$$\mathcal{N}_m = [0.2, 4] \text{ kg}, \quad \mathcal{N}_b = [1.7, 34] \text{ N} \cdot \text{s/m} \quad (40)$$

for m and b , respectively.

C. Experimental results and discussion

This section presents the results of the experiments performed based on the three exercises shown in Fig. 10. In particular, the analysis was focused on the impact that the choice of parameters m and b has on the human-robot interaction mediated by a DMP-based admittance control. Figure 11 and Figure 12 display the outcomes from tasks (a) and (b). They were executed for 60 s by different users,

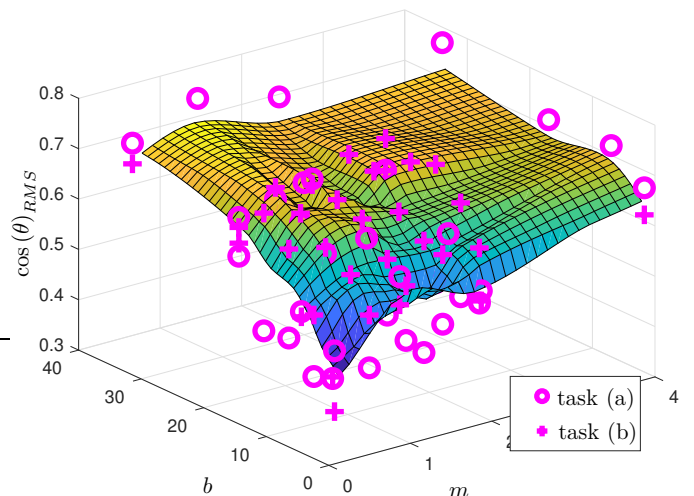


Figure 11: Trend analysis of the external force application angle $\cos(\theta)_{\text{RMS}}$.

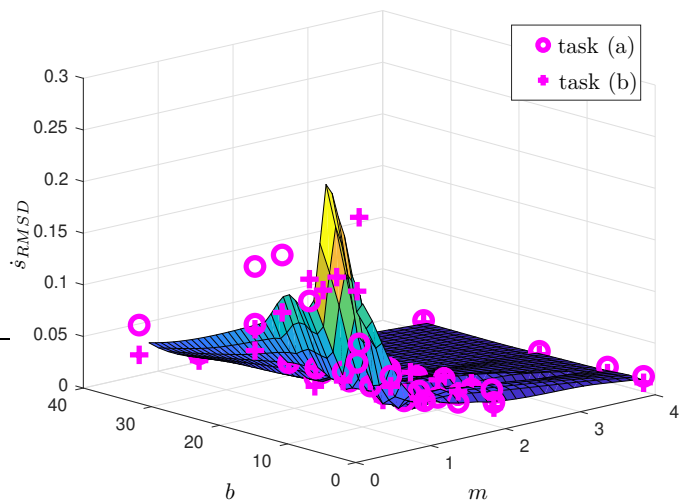


Figure 12: Trend analysis of the peak-to-peak oscillations on phase velocity $\dot{s}(t)$.

who were required to move forward and backward along the trajectory defined by the GDMP. In each trial, random values of $b \in \mathcal{N}_b$ and $m \in \mathcal{N}_m$ were assumed.

In the two figures, each magenta marker represents the result of an experiment (circles correspond to task (a), while crosses denote task (b)). In Figure 11, we examine the (cosine of the) angle between the force \mathbf{F}_h exerted by the user and the tangent direction to the curve generated by the DMP. This metric represents the ratio between the magnitude of the tangent component and the norm of the force \mathbf{F}_h :

$$\cos(\theta(t)) = \frac{F_\tau(t)}{\|\mathbf{F}_h(t)\|}.$$

To condense the information contained within the profile of $\cos(\theta(t))$ recorded during a trial into a single point, we consider the Root Mean Square (RMS) value. This parameter is significant because it reflects the user's ability to move the robot EE along the trajectory encoded by the GDMP with minimal tangent force. As illustrated

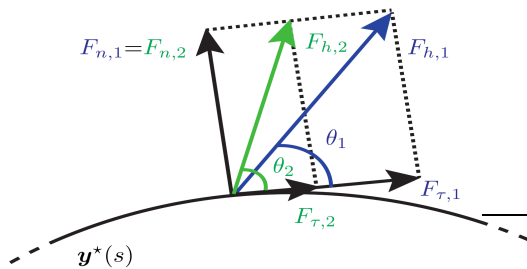


Figure 13: Variation of θ with respect to different applied forces \mathbf{F}_h .

in Fig. 13, with a constant normal force component $F_{n,1} = F_{n,2}$, reducing the tangent force component leads to an increase in the angle θ and consequently a decrease in $\cos(\theta)$, which tends to zero as F_τ approaches zero. Therefore, this parameter serves as a reliable measure of the magnitude of the tangent force applied by the user, with the advantage of always being within the range $[0, 1]$ and not being dependent on the magnitude of force applied by a particular user.

The plot in Fig. 11, illustrating the surface approximating the points obtained from all the trials as a function of m and b , suggests that, as expected, lower values of these parameters decrease the effort required for the user to execute the task. However, this choice may lead to significant instability issues during human-robot interaction, such as vibrations and oscillations. Figure 12 precisely demonstrates this system trend, illustrating the Root Mean Square Deviation (RMSD) of the velocity along the trajectory concerning the average value as a function of $m \in \mathcal{N}_m$ and $b \in \mathcal{N}_b$:

$$\dot{s}_{RMSD} = \text{rms}(\dot{s}(t) - \dot{s}(t)_{AVG}), \quad (41)$$

where $\dot{s}(t)_{AVG}$ represents the moving average of the function $\dot{s}(t)$ over a window of 0.1 seconds. This metric quantifies the average magnitude of the oscillations affecting the phase velocity $\dot{s}(t)$ across various tasks. From the figure, it is noticeable that decreasing b and m results in an increase in the \dot{s}_{RMSD} metric. This implies that the average oscillations affecting the phase variable $s(t)$ become more pronounced, ultimately leading to the robot's stoppage due to the breach of safe limit constraints. This trend is evident in Fig. 14, where two different sets of parameters m and b are considered during the execution of the task (c) in Fig. 10c. The figure displays the phase $s(t)$ and the power $P_\tau(t) = F_\tau(t) \cdot \dot{s}(t)$ exchanged between human and robot during motion along the trajectory defined by the GDMP. It is important to note that in this task, the user is required to halt at the position corresponding to $s(t) \approx 0.42$ m. For "large" values of m and b ($m = 2$, $b = 17$), the user manages to guide the robot along the trajectory with a limited amount of power. Conversely, with "small" values of m and b ($m = 0.2$, $b = 7$), which fall within the yellow peak of the plot in Fig. 12, the signal $s(t)$ displays pronounced oscillations, especially when reaching the stop position. Consequently, the human user attempts to counteract

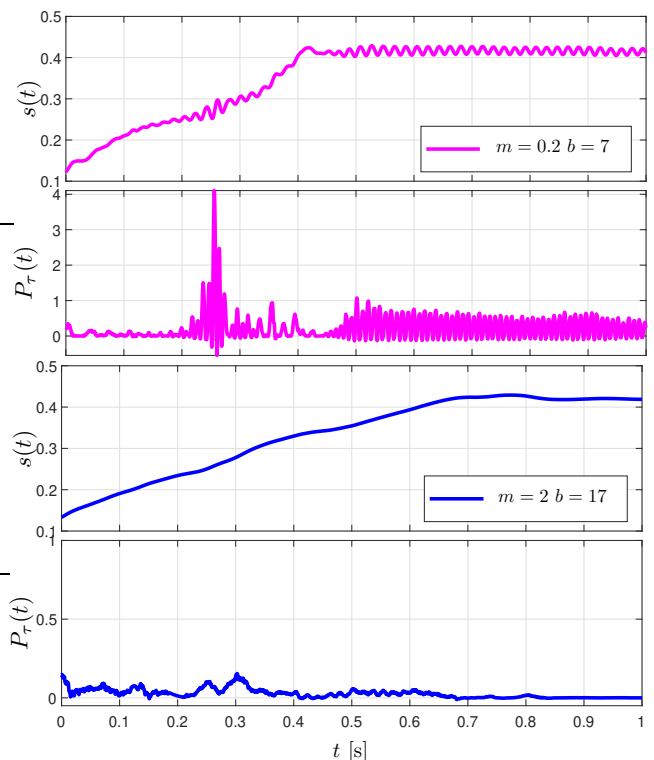


Figure 14: Comparison between the behaviors obtained in the task (c) with different parameters m and b .

the robot's oscillations, thereby generating a substantial amount of power, as depicted in the figure. This behavior could potentially lead to escalating instability issues, despite, according to the stability proof outlined in Sec. VI, the system should be stable for any positive value of m and b . This mismatch might stem from the assumptions made in the analysis. Specifically, in the control scheme depicted in Fig. 8, we neglected the robot dynamics, presuming that position control guarantees perfect tracking of the reference trajectory, i.e., $\mathbf{y}_m(t) = \mathbf{y}(t)$. To align more closely with reality, a non-ideal aspect was introduced by considering a finite delay t_0 in the generation of the desired position by the robot manipulator, i.e., $\mathbf{y}_m(t) = \mathbf{y}(t - t_0)$. This delay in the feedback loop renders the system non-passive. Consequently, in order to analyze the system stability, alternative tools beyond passivity analysis are necessary. For this reason, Lyapunov's indirect method has been employed, considering a linear approximation of the system [52]. To allow this analysis, a model of the human interacting with the robot has been introduced. Providing an accurate description of the human is non-trivial [54]. However, for the purposes of this analysis, the human can be simplified as a spring-damper system, exhibiting isotropic behavior across all spatial directions:

$$\underbrace{\begin{bmatrix} F_{h_x} \\ F_{h_y} \\ F_{h_z} \end{bmatrix}}_{\mathbf{F}_h} = \underbrace{\begin{bmatrix} G_h(s_l) & 0 & 0 \\ 0 & G_h(s_l) & 0 \\ 0 & 0 & G_h(s_l) \end{bmatrix}}_{\mathbf{G}_h(s_l)} \underbrace{\begin{bmatrix} \dot{y}_{a_x} \\ \dot{y}_{a_y} \\ \dot{y}_{a_z} \end{bmatrix}}_{\dot{\mathbf{y}}_m}, \quad \text{where } G_h(s_l) = \frac{B_h s_l + K_h}{s_l}, \quad (42)$$

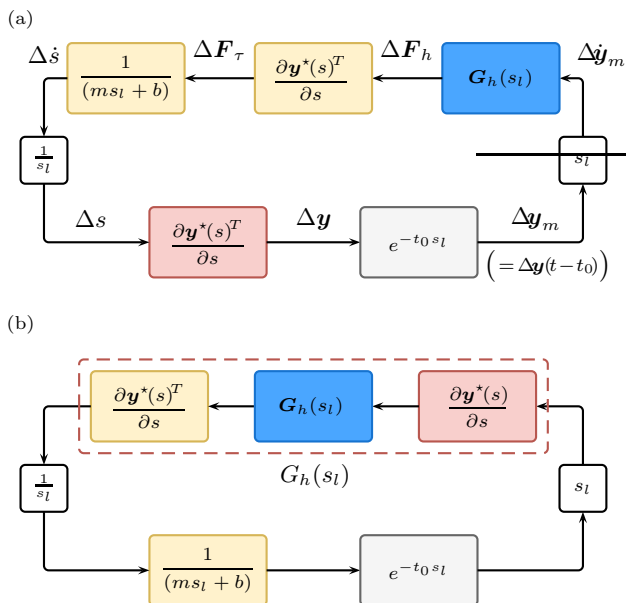


Figure 15: Human-robot interaction through kinesthetic guidance: Linearization.

being s_l the Laplace complex variable.

Assuming the GDMP behaves as an ideal trajectory generator, i.e., $\mathbf{y}(t) \approx \mathbf{y}^*(s(t))$, and linearizing the scheme depicted in Fig. 8 for small variations around the equilibrium point $(s_e, \dot{s}_e) = (\bar{s}, 0)$, where \bar{s} represents the stop position, we can derive the scheme illustrated in Fig. 15a. Moreover, as the model in Fig. 15a is linear, rearranging the block order yields a simplified linear representation of the system as shown in Fig. 15b. It is important to note that the blocks enclosed by the red dashed line in Fig. 15b ultimately reduce to the scalar gain $G_h(s_l)$:

$$\frac{\partial \mathbf{y}^*(s)^T}{\partial s} \mathbf{G}_h(s_l) \frac{\partial \mathbf{y}^*(s)}{\partial s} = G_h(s_l) \underbrace{\left\| \frac{\partial \mathbf{y}^*(s)}{\partial s} \right\|^2}_{\approx 1 \text{ from (21)}}.$$

Thanks to the considerations above, one can conclude that the linearized representation of the system in Fig. 8, i.e. Fig. 15b, is characterized by the following input-output transfer function:

$$G_{IO}(s_l) = \frac{G_{LG}(s_l)}{1 + G_{LG}(s_l)} \quad \text{with} \quad (43)$$

$$G_{LG}(s_l) = \frac{G_h(s_l)e^{-t_0 s_l}}{ms_l + b} = \frac{(B_h s_l + K_h)e^{-t_0 s_l}}{s_l(ms_l + b)},$$

and where G_{LG} stands for the loop-gain function of the system G_{IO} .

The qualitative Nyquist diagram of the loop-gain function $G_{LG}(s_l)$ in (43) is shown in Fig. 16. The presence of a finite delay t_0 causes the Nyquist diagram of $G_{LG}(s_l)$ not to be confined in the Right Half-Plane. This confirms that the passivity of the system in Fig. 8, which has been proven in Sec. VI-A with respect to the energetic port $P_T = \dot{\mathbf{y}}_m^T(t) \mathbf{F}_h(t)$, does not hold if $\dot{\mathbf{y}}_m(t) = \dot{\mathbf{y}}(t - t_0)$ [52].

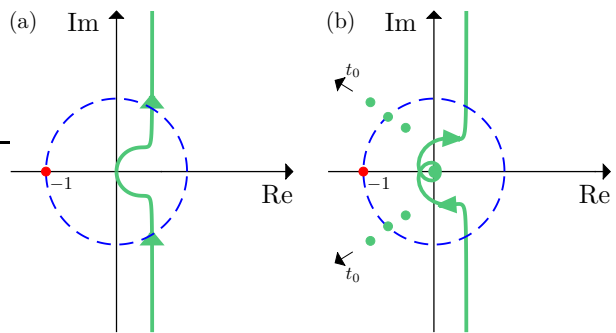


Figure 16: Nyquist diagram of the loop-gain function $G_{LG}(s_l)$ without (a) and with (b) finite delay t_0 .

As the delay t_0 increases, the portion of the Nyquist contour in the Left Half-Plane (LHP) grows. However, based on the Nyquist criterion, the closed-loop system remains stable as long as the Nyquist contour of $G_{LG}(s_l)$ does not touch or encircle the critical point $-1 + j0$ [55]. It is important to note that the system $G_{LG}(s_l)$ is minimum-phase. Common metrics for assessing the stability of the system are the so-called stability margins, specifically the gain and phase margins [55]. Given the presence of the delay in the loop function, particular emphasis is placed on the phase margin M_φ . To ensure the stability of the closed-loop system $G_{IO}(s_l)$, the phase margin of the loop function must be positive. As depicted in Fig. 17, when the robot position control is unaffected by a delay ($t_0 = 0$), the phase margin remains positive. However, as the delay increases, M_φ decreases, especially for small values of m and b . In these cases, the situation becomes critical, as observed in the experimental tests.

As a general guideline, when selecting the parameters for the second-order filter that generates the phase variable $s(t)$, it is crucial to emphasize that both m and b must have non-negligible values to ensure the stability of the human-in-the-loop system with an admittance-based DMP architecture. On the contrary with respect to what energy considerations might suggest, it is not sufficient to focus solely on the damping parameter b .

VIII. CONCLUSIONS

The Canonical System of the DMP informs the evolution of the forcing term, shaping the attractor landscape for desired output dynamics. While standard DMPs ensure time modulation, no unified framework exists in the literature to compactly handle multiple phase profiles without significantly altering the standard DMP formulation. In this study, we address this by introducing Geometric Dynamic Motion Primitives (GDMP), which leverages a spatial sampling algorithm to decouple the learned curve from its timing law, based on the arc-length parameter of the task curve.

We demonstrate this framework in a simulated environment, by optimizing the phase profile to minimize task execution time while respecting velocity and acceleration constraints. More importantly, we apply our methodology

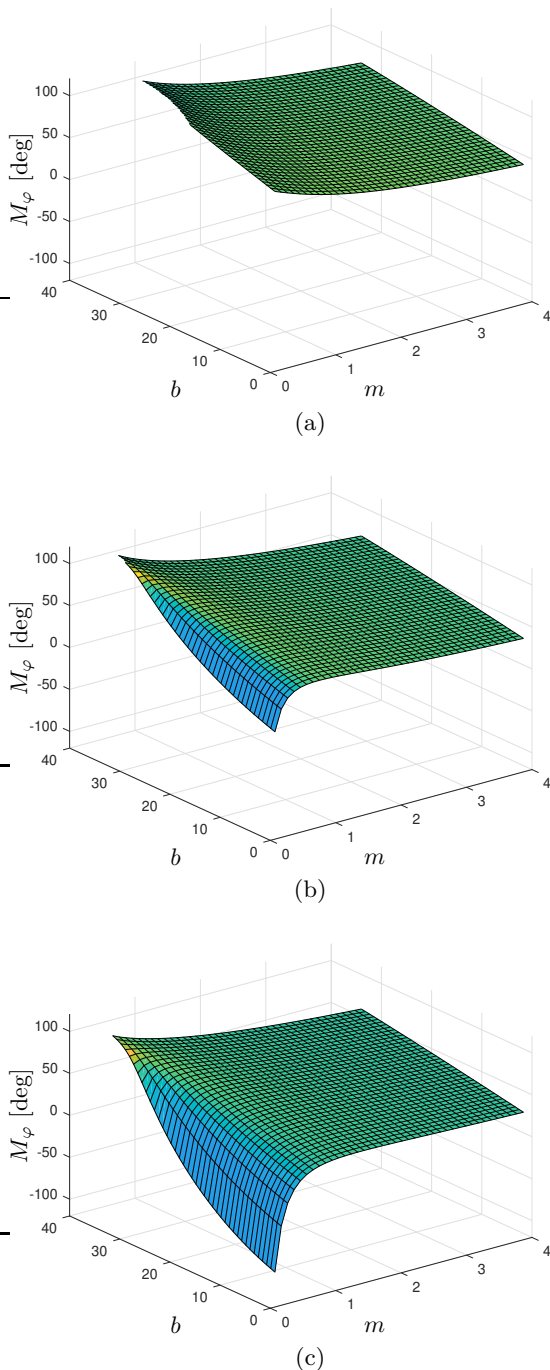


Figure 17: Phase margin M_φ of the loop-gain function $G_{LG}(s_l)$ as a function of m , b for different values of the delay t_0 : $t_0=0$ s (a), $t_0=0.01$ s (b), and $t_0=0.02$ s (c).

to a co-manipulation scenario involving a human physically interacting with the robot End-effector, guiding the system forward and backward along the trajectories encoded by the DMP. By designing a custom phase law and conducting various real-world experiments with different parameter values, we identified potential stability issues that were not anticipated during the passivity analysis. This analysis was necessary due to the closed-loop structure involving the robot tracking the output trajectory of the DMP generated based on the interaction of the user

with the robot itself.

A general guideline for selecting the parameters of the phase filter, based on experimental tests and theoretical considerations, is finally provided.

APPENDIX A

CLOSED-FORM SOLUTION FOR THE COMPUTATION OF THE WEIGHTS VECTOR

The optimal control problem (12) can be written in a matrix form as:

$$\boldsymbol{\omega} = \underset{\boldsymbol{\omega}}{\operatorname{argmin}} \|\mathbf{y}_r - \boldsymbol{\Psi}^T \boldsymbol{\omega}\|^2, \quad (44)$$

where $\boldsymbol{\omega} \in \mathbb{R}^{(N \times 1)}$ and:

$$\boldsymbol{\Psi} = \begin{bmatrix} \phi_1(s(0)) \cdots \phi_1(s(T_f)) \\ \phi_2(s(0)) \cdots \phi_2(s(T_f)) \\ \vdots \quad \ddots \quad \vdots \\ \phi_N(s(0)) \cdots \phi_N(s(T_f)) \end{bmatrix}, \quad \mathbf{y}_r = \begin{bmatrix} y_r(0) \\ \cdots \\ y_r(T_f) \end{bmatrix}, \quad (45)$$

with $\boldsymbol{\Psi} \in \mathbb{R}^{(N \times T_f)}$ and $\mathbf{y}_r \in \mathbb{R}^{(T_f \times 1)}$. The constraints (13) can be written in a matrix form as:

$$\mathbf{C}\boldsymbol{\omega} = \mathbf{H}, \quad \text{where}$$

$$\mathbf{C} = \begin{bmatrix} \boldsymbol{\Phi}(s(0))^T \\ \boldsymbol{\Phi}(s(T_f))^T \end{bmatrix}, \quad \mathbf{H} = \begin{bmatrix} y_r(0) \\ g_r \end{bmatrix}, \quad (46)$$

and $\boldsymbol{\Phi}(s(t)) = [\phi_1(s(t)), \phi_2(s(t)), \dots, \phi_N(s(t))]^T$. Note that, during the learning of weights $\boldsymbol{\omega}$, we assumed the reference goal $g_r = y_r(T_f)$.

The optimal control problem (44) subject to (46) represents a constrained least-squares minimization problem, which can be analytically solved using the Lagrange multipliers method [12]. Specifically, (44) subject to (46) is the same as solving:

$$\operatorname{tr} \left[(\mathbf{y}_r - \boldsymbol{\Psi}^T \boldsymbol{\omega})^T \mathbf{Q} (\mathbf{y}_r - \boldsymbol{\Psi}^T \boldsymbol{\omega}) + \boldsymbol{\lambda}^T (\mathbf{C}\boldsymbol{\omega} - \mathbf{H}) \right], \quad (47)$$

being $\boldsymbol{\lambda} = [\lambda_1, \lambda_2]^T$ the vector of Lagrange multipliers, $\mathbf{Q} \in \mathbb{R}^{(T_f \times T_f)}$ is precision matrix over the approximation constraint and “ tr ” denotes the trace operator. By differentiating (47) and equating it to zero, after some algebraic manipulations one obtains:

$$\begin{aligned} \boldsymbol{\Psi} \mathbf{Q} \boldsymbol{\Psi}^T \boldsymbol{\omega} + \mathbf{C}^T \boldsymbol{\lambda} &= \boldsymbol{\Psi} \mathbf{Q} \mathbf{y}_r, \\ \mathbf{C} \boldsymbol{\omega} &= \mathbf{H}. \end{aligned} \quad (48)$$

If matrices $\mathbf{P} = \boldsymbol{\Psi} \mathbf{Q} \boldsymbol{\Psi}^T$ and $\mathbf{R} = \mathbf{C} (\boldsymbol{\Psi} \mathbf{Q} \boldsymbol{\Psi}^T)^{-1} \mathbf{C}^T$ are both invertible, the solution of (48) boils down to:

$$\begin{aligned} \boldsymbol{\lambda} &= \mathbf{R}^{-1} (\mathbf{C} \mathbf{P}^{-1} \boldsymbol{\Psi} \mathbf{Q} \mathbf{y}_r - \mathbf{H}), \\ \boldsymbol{\omega} &= \mathbf{P}^{-1} \boldsymbol{\Psi} \mathbf{Q} \mathbf{y}_r - \mathbf{P}^{-1} \mathbf{C}^T \boldsymbol{\lambda}, \end{aligned}$$

providing the optimal weights vector $\boldsymbol{\omega}$ solving the constrained optimisation problem (44) subject to (46).

APPENDIX B

SPATIAL SAMPLING ALGORITHM

The MATLAB-like form the the Spatial Sampling algorithm is shown in Fig. 18. The codes for this paper are publicly available in the attached material.

```

function [ $s_k, t_\Delta, Y_{\Delta,k}^T$ ] = SpatialSampling( $\Delta, t_T, Y_T^T$ )
1.  $s_k = [0]$ ; % phase vector of Spatially-Sampled Trajectory (SST)
2.  $t_\Delta = [0]$ ; % time samples of Spatially-Sampled Trajectory (SST)
3.  $n_t = \text{size}(Y_T, 1)$ ; % nr of samples in the Demonstrated Trajectory (DT)
4.  $n_s = \text{size}(Y_T, 2)$ ; % nr of components in DT
5.  $y_c = Y_T(1, :)$ ; % initialize  $y_c$ , containing the SST latest samples
6.  $Y_{\Delta,k} = y_c$ ; % SST provided as output
7. for  $i = 1 : n_t - 1$  % cycle over DT samples
8.  $\overline{\Delta}_{y_{Tc}} = \|Y_T(i+1, :) - y_c\|$ ; % norm of vector  $Y_T(i+1, :) - y_c$ 
9. if  $\overline{\Delta}_{y_{Tc}} > \Delta$  % spatial sampling applied if this is verified
10.  $n_{sst} = \text{floor}(\overline{\Delta}_{y_{Tc}}/\Delta)$ ; % nr of new samples to be introduced in SST
11. for  $p = 1 : n_{sst}$  % cycle over number  $n_{sst}$ 
12.  $s_k = [s_k; s_k(\text{end}) + \Delta]$ ; % compute the phase of SST
13.  $y_{in} = \text{zeros}(1, n_s)$ ; % initialize new samples of SST components
14. for  $j = 1 : n_s$  % cycle over DT components
15.  $\Delta_{Y_T} = (Y_T(i+1, j) - y_c(j))/\overline{\Delta}_{y_{Tc}}$  % normalized movement along j-th SST component
16.  $y_{in}(j) = y_c(j) + \Delta * \Delta_{Y_T}$  % store new sample of j-th SST component
17. end
18.  $Y_{\Delta,k} = [Y_{\Delta,k}; y_{in}]$ ; % update SST provided as output
19.  $y_c = y_{in}$ ; % update latest samples of SST components
20.  $\overline{\Delta}_{y_{TT}} = \|Y_T(i+1, :) - Y_T(i, :)\|$ ; % norm of vector  $Y_T(i+1, :) - Y_T(i, :)$ 
21.  $\overline{\Delta}_t = t_T(i+1) - t_T(i)$ ; % time spacing  $t_T(i+1) - t_T(i)$  in DT
22.  $m = \overline{\Delta}_{y_{TT}}/\overline{\Delta}_t$ ; % slope of line  $\overline{\Delta}_{y_{TT}}$  vs  $\overline{\Delta}_t$ 
23.  $t_\Delta = [t_\Delta; (\|y_c - Y_T(i, :)\| + m * t_T(i))] / m$ ; % update time vector of the SST
24. end
25. end
26. end

```

Figure 18: MATLAB-like form of the Spatial Sampling algorithm.

REFERENCES

- [1] A. M. Zanchettin, N. M. Ceriani, P. Rocco, H. Ding, and B. Matthias, "Safety in human-robot collaborative manufacturing environments: Metrics and control," *IEEE Transactions on Automation Science and Engineering*, vol. 13, no. 2, pp. 882–893, 2015.
- [2] L. Zhang, S. Guo, and Q. Sun, "Development and assist-needed control of an end-effector upper limb rehabilitation robot," *Applied Sciences*, vol. 10, no. 19, p. 6684, 2020.
- [3] K. Merckaert, B. Convens, C.-j. Wu, A. Roncone, M. M. Nicotra, and B. Vanderborght, "Real-time motion control of robotic manipulators for safe human-robot coexistence," *Robotics and Computer-Integrated Manufacturing*, vol. 73, p. 102223, 2022.
- [4] A. D. Deshpande, "Novel biomedical technologies: Rehabilitation robotics," *Current Opinion in Biomedical Engineering*, vol. 22, 2022.
- [5] C. Lauretti, F. Cordella, E. Guglielmelli, and L. Zollo, "Learning by demonstration for planning activities of daily living in rehabilitation and assistive robotics," *IEEE Robotics and Automation Letters*, vol. 2, no. 3, pp. 1375–1382, 2017.
- [6] N. Hogan and D. Sternad, "Dynamic primitives in the control of locomotion," *Frontiers in computational neuroscience*, vol. 7, p. 71, 2013.
- [7] S. Calinon, F. Guenter, and A. Billard, "On learning, representing, and generalizing a task in a humanoid robot," *IEEE Transactions on Systems, Man, and Cybernetics, Part B (Cybernetics)*, vol. 37, no. 2, pp. 286–298, 2007.
- [8] S. Calinon, *Robot programming by demonstration*. EPFL Press, 2009.
- [9] S. Schaal, "Is imitation learning the route to humanoid robots?" *Trends in cognitive sciences*, vol. 3, no. 6, pp. 233–242, 1999.
- [10] G. E. Hovland, P. Sikka, and B. J. McCarragher, "Skill acquisition from human demonstration using a hidden markov model," in *Proceedings of IEEE international conference on robotics and automation*, vol. 3. Ieee, 1996, pp. 2706–2711.
- [11] L. Sciavicco, B. Siciliano, L. Villani, and G. Oriolo, "Robotics: Modelling, planning and control, ser. advanced textbooks in control and signal processing," 2011.
- [12] L. Biagiotti and C. Melchiorri, *Trajectory Planning for Automatic Machines and Robots*. Springer, 2008.
- [13] M. Saveriano, F. J. Abu-Dakka, A. Kramberger, and L. Pernel, "Dynamic movement primitives in robotics: A tutorial survey," *arXiv preprint arXiv:2102.03861*, 2021.
- [14] A. J. Ijspeert, J. Nakanishi, H. Hoffmann, P. Pastor, and S. Schaal, "Dynamical movement primitives: Learning attractor models for motor behaviors," *Neural Computation*, vol. 25, no. 2, pp. 328–373, 2013.
- [15] A. Ijspeert, J. Nakanishi, and S. Schaal, "Movement imitation with nonlinear dynamical systems in humanoid robots," in *Proceedings 2002 IEEE International Conference on Robotics and Automation (Cat. No.02CH37292)*, vol. 2, 2002, pp. 1398–1403 vol.2.
- [16] R. L. Devaney, "Reversible diffeomorphisms and flows," *Transactions of the American Mathematical Society*, vol. 218, pp. 89–113, 1976.
- [17] C. Atkeson, "Using local models to control movement," *Advances in neural information processing systems*, vol. 2, 1989.
- [18] P. Pastor, H. Hoffmann, T. Asfour, and S. Schaal, "Learning and generalization of motor skills by learning from demonstration," in *2009 IEEE International Conference on Robotics and Automation*, 2009, pp. 763–768.
- [19] B. Nemeč, A. Gams, M. Deniša, and A. Ude, "Human-robot cooperation through force adaptation using dynamic motion primitives and iterative learning," in *2014 IEEE International Conference on Robotics and Biomimetics (ROBIO 2014)*, 2014, pp. 1439–1444.
- [20] A. Sidiropoulos and Z. Doulgeri, "A reversible dynamic movement primitive formulation," in *2021 IEEE International Conference on Robotics and Automation (ICRA)*, 2021, pp. 3147–3153.

- [21] B. Nemeč, A. Gams, and A. Ude, "Velocity adaptation for self-improvement of skills learned from user demonstrations," in *2013 13th IEEE-RAS International Conference on Humanoid Robots (Humanoids)*, 2013, pp. 423–428.
- [22] E. A. Rückert and A. d'Avella, "Learned parametrized dynamic movement primitives with shared synergies for controlling robotic and musculoskeletal systems," *Frontiers in Computational Neuroscience*, vol. 7, 2013.
- [23] A. Sidiropoulos and Z. Doulgeri, "Dynamic via-points and improved spatial generalization for online trajectory planning with dynamic movement primitives," <https://arxiv.org/abs/2212.13473>, 2023.
- [24] B. Kiss and E. Szádeczky-Kardoss, "Time-scaling in the control of mechatronic systems," *New Developments in Robotics Automation and Control*, pp. 411–426, 2008.
- [25] M. Sampei and K. Furuta, "On time scaling for nonlinear systems: Application to linearization," *IEEE Transactions on Automatic Control*, vol. 31, no. 5, pp. 459–462, 1986.
- [26] R. Samant, L. Behera, and G. Pandey, "Adaptive learning of dynamic movement primitives through demonstration," in *2016 International Joint Conference on Neural Networks (IJCNN)*, 2016, pp. 1068–1075.
- [27] T. Kulvicius, K. Ning, M. Tamosiunaite, and F. Wörgötter, "Modified dynamic movement primitives for joining movement sequences," in *2011 IEEE International Conference on Robotics and Automation*. IEEE, 2011, pp. 2275–2280.
- [28] B. Nemeč, M. Simonič, T. Petrič, and A. Ude, "Incremental policy refinement by recursive regression and kinesthetic guidance," in *2019 19th International Conference on Advanced Robotics (ICAR)*, 2019, pp. 344–349.
- [29] A. Kramberger, E. Shahriari, A. Gams, B. Nemeč, A. Ude, and S. Haddadin, "Passivity based iterative learning of admittance-coupled dynamic movement primitives for interaction with changing environments," in *2018 IEEE/RSJ International Conference on Intelligent Robots and Systems (IROS)*. IEEE, 2018, pp. 6023–6028.
- [30] B. Nemeč, A. Ude *et al.*, "Speed adaptation for self-improvement of skills learned from user demonstrations," *Robotica*, vol. 34, no. 12, pp. 2806–2822, 2016.
- [31] G. Braglia, M. Tagliavini, F. Pini, and L. Biagiotti, "Online motion planning for safe human-robot cooperation using b-splines and hidden markov models," *MDPI Robotics*, vol. 12, no. 4, 2023.
- [32] D. Verscheure, B. Demeulenaere, J. Swevers, J. De Schutter, and M. Diehl, "Time-optimal path tracking for robots: A convex optimization approach," *IEEE Transactions on Automatic Control*, vol. 54, no. 10, pp. 2318–2327, 2009.
- [33] B. Nemeč, L. Žlajpah, S. Šlajpa, J. Piškur, and A. Ude, "An efficient pbd framework for fast deployment of bi-manual assembly tasks," in *2018 IEEE-RAS 18th International Conference on Humanoid Robots (Humanoids)*. IEEE, 2018, pp. 166–173.
- [34] I. Iturrate, C. Sloth, A. Kramberger, H. G. Petersen, E. H. Østergaard, and T. R. Savarimuthu, "Towards reversible dynamic movement primitives," in *2019 IEEE/RSJ International Conference on Intelligent Robots and Systems (IROS)*, 2019, pp. 5063–5070.
- [35] A. Sidiropoulos, D. Papageorgiou, and Z. Doulgeri, "A novel framework for generalizing dynamic movement primitives under kinematic constraints," *Autonomous Robots*, vol. 47, no. 1, pp. 37–50, 2023.
- [36] L. Koutras and Z. Doulgeri, "A novel dmp formulation for global and frame independent spatial scaling in the task space," in *2020 29th IEEE International Conference on Robot and Human Interactive Communication (RO-MAN)*. IEEE, 2020, pp. 727–732.
- [37] S. Wiggins, S. Wiggins, and M. Golubitsky, *Introduction to applied nonlinear dynamical systems and chaos*. Springer, 2003, vol. 2, no. 3.
- [38] H. Zhao, Y. Chen, X. Li, and H. Ding, "Robotic peg-in-hole assembly based on reversible dynamic movement primitives and trajectory optimization," *Mechatronics*, vol. 95, p. 103054, 2023.
- [39] J. Jankowski, L. Bruder Müller, N. Hawes, and S. Calinon, "Vp-sto: Via-point-based stochastic trajectory optimization for reactive robot behavior," in *2023 IEEE International Conference on Robotics and Automation (ICRA)*. IEEE, 2023, pp. 10 125–10 131.
- [40] G. Raiola, X. Lamy, and F. Stulp, "Co-manipulation with multiple probabilistic virtual guides," in *2015 IEEE/RSJ international conference on intelligent robots and systems (IROS)*. IEEE, 2015, pp. 7–13.
- [41] S. S. Restrepo, G. Raiola, P. Chevalier, X. Lamy, and D. Sidobre, "Iterative virtual guides programming for human-robot co-manipulation," in *2017 IEEE International conference on advanced intelligent mechatronics (AIM)*. IEEE, 2017, pp. 219–226.
- [42] H. B. Amor, G. Neumann, S. Kamthe, O. Kroemer, and J. Peters, "Interaction primitives for human-robot cooperation tasks," in *2014 IEEE international conference on robotics and automation (ICRA)*. IEEE, 2014, pp. 2831–2837.
- [43] D. J. Berndt and J. Clifford, "Using dynamic time warping to find patterns in time series," in *Proceedings of the 3rd international conference on knowledge discovery and data mining*, 1994, pp. 359–370.
- [44] L. Biagiotti and C. Melchiorri, "Online trajectory planning and filtering for robotic applications via b-spline smoothing filters," in *2013 IEEE/RSJ International Conference on Intelligent Robots and Systems*. IEEE, 2013, pp. 5668–5673.
- [45] A. Kanazawa, J. Kinugawa, and K. Kosuge, "Adaptive motion planning for a collaborative robot based on prediction uncertainty to enhance human safety and work efficiency," *IEEE Transactions on Robotics*, vol. 35, no. 4, pp. 817–832, 2019.
- [46] H. Gattringer, A. Mueller, M. Oberherber, and D. Kaserer, "Time-optimal robotic manipulation on a predefined path of loosely placed objects: Modeling and experiment," *Mechatronics*, vol. 84, p. 102753, 2022.
- [47] "Franka Emika next generation robotics," <https://www.franka.de/>, accessed: 2022-07-26.
- [48] J. A. E. Andersson, J. Gillis, G. Horn, J. B. Rawlings, and M. Diehl, "CasADi – A software framework for nonlinear optimization and optimal control," *Mathematical Programming Computation*, vol. 11, no. 1, pp. 1–36, 2019.
- [49] M. Simonič, T. Petrič, A. Ude, and B. Nemeč, "Analysis of methods for incremental policy refinement by kinesthetic guidance," *Journal of Intelligent & Robotic Systems*, vol. 102, no. 1, pp. 1–19, 2021.
- [50] A. Q. Keemink, H. van der Kooij, and A. H. Stienen, "Admittance control for physical human-robot interaction," *The International Journal of Robotics Research*, vol. 37, no. 11, pp. 1421–1444, 2018. [Online]. Available: <https://doi.org/10.1177/0278364918768950>
- [51] D. Tebaldi and R. Zanasi, "A unified methodology for the power efficiency analysis of physical systems," *Journal of the Franklin Institute*, vol. 361, no. 1, pp. 283–300, 2024.
- [52] H. K. Khalil, "Nonlinear systems third edition," *Patience Hall*, vol. 115, 2002.
- [53] E. Colgate and N. Hogan, "The interaction of robots with passive environments: Application to force feedback control," in *Advanced Robotics: 1989: Proceedings of the 4th International Conference on Advanced Robotics Columbus, Ohio, June 13–15, 1989*. Springer, 1989, pp. 465–474.
- [54] F. Ficuciello, A. Romano, L. Villani, and B. Siciliano, "Cartesian impedance control of redundant manipulators for human-robot co-manipulation," in *2014 IEEE/RSJ international conference on intelligent robots and systems*. IEEE, 2014, pp. 2120–2125.
- [55] K. Ogata, *Modern Control Engineering*. Prentice Hall, 2010.